ELECTROCHEMISTRY OF ELECTROLESS PLATING ON OPTICAL FIBER FOR SENSORS AND VANADIUM SULFIDE CATHODES FOR BATTERIES

by

James C. Egbu, Jr., B.S.

A thesis submitted to the Graduate Council of
Texas State University in partial fulfillment
of the requirements for the degree of
Master of Science
with a Major in Chemistry
August 2019

Committee Members:

Benjamin R. Martin, Chair

Ruishu F. Wright

Todd W. Hudnall

Christopher P. Rhodes

FAIR USE AND AUTHOR'S PERMISSION STATEMENT

Fair Use

Duplication Permission

DEDICATION

To my son

James C. Egbu, III

ACKNOWLEDGEMENTS

The research on electroless plating on optical fiber for corrosion sensors was supported by an appointment at the National Energy Technology Laboratory, sponsored by the US Department of Energy's Mickey Leland Energy Fellowship Program and administered by the Oak Ridge Institute for Science and Education.

The research on optical fiber-based water monitoring sensors was supported by an appointment to the National Energy Technology Laboratory Research Participation Program, sponsored by the U.S. Department of Energy and administered by the Oak Ridge Institute for Science and Education.

The research on ion intercalation into vanadium sulfides was supported by the National Science Foundation PREM Center DMR-1205670.

I would like to thank Dr. Benjamin Martin for making any of this work possible. Thank you for your guidance, mentorship, motivation, knowledge, intellectual opinions, and for allowing me to grow as a researcher, I am very grateful.

I would equally like to thank Dr. Ruishu Wright. Dr. Wright, thank you for letting me work with you on such an important scientific topic as corrosion. Your immense knowledge, command over this topic, and guidance have made me a more competent researcher. Thank you for mentoring me and also allowing me some independence to grow.

My sincere gratitude to my thesis committee members, Dr. Todd Hudnall and Dr. Christopher Rhodes. Dr. Hudnall, thank you for your words of encouragement and support throughout my graduate studies at Texas State. Dr. Rhodes, thank you for the discussions on electrochemistry and your contributions that made this thesis better.

I am grateful to Dr. Paul Ohodnicki, Jr., for his support and giving me the opportunity to conduct part of this thesis research at the National Energy Technology Laboratory in Pittsburgh, PA. Thank you to all of the scientists at the Advanced Sensor Development Lab and co-authors on some of this work – Dr. Ping Lu, thank you for the lively discussions on optical fibers, Dr. Fei Lu, Dr. Jeff Culp, Dr. Michael Buric, Dr. Mudabbir Badar.

To my friends mentioned and those not mentioned here, I am grateful for your support. Especially, Valentine Nnamah, Jacob Armitage, Chinonye Ogbonnaya-Odor, M.D., and Celia Mimms, D.D.S.

Finally, I would like to thank my parents, James and Nnenna Egbu, and my siblings, Gloria, Obinna, and Agharandu, for all their love and support. Again, to my mother, thank you for sparking my desire to become a scientist. Thank you all!

Publications Resulting from the Work in this Thesis

This thesis consists of work related to the following published and yet to be published research as listed below:

1. **Egbu, J**.; Martin, B. Ion Intercalation into Vanadium Sulfides for Battery Applications. *ECS Meet. Abstr.* 2018, *MA2018-03* (4), 251–251.

2. Wright, R. F.; **Egbu, J**.; Lu, P.; Buric, M.; Ziomek-Moroz, M.; Ohodnicki, P. R. J. Electrolessly Coated Optical Fibers for Distributed Corrosion Monitoring. In *CORROSION 2019*; NACE International: Nashville, 2019; No. 13499.

3. Wright, R. F.; **Egbu, J**.; Lu, P.; Ziomek-Moroz, M.; Ohodnicki, P. R. J. Optical Fiber-Based Corrosion Sensor with Fe/SiO_2 Coating. (Manuscript)

4. Wright, R.; Badar, M.; **Egbu, J**. C.; Lu, P.; Buric, M. P.; Ohodnicki, P. R. Fully Distributed Optical Fiber Sensor for Water and Humidity Monitoring. In *Fiber Optic Sensors and Applications XVI*; SPIE, 2019; Vol. 11000, 6.

TABLE OF CONTENTS

Page

LIST OF TABLES

Table **Page**

LIST OF FIGURES

Figure **Page**

LIST OF ABBREVIATIONS

Abbreviation	Description
SEM	Scanning Electron Microscope
XPS	X-ray Photoelectron Spectroscopy
OBR	Optical Backscatter Reflectometer
SM	Single Mode
SHE	Standard Hydrogen Electrode
EDA-Si	3-(2-aminoethyl amino)-propyl-trimethoxy silane
ENP	Electroless Nickel Plating
ECP	Electroless Copper Plating
PHMSA	The Pipeline and Hazardous Materials Safety Administration
DI water	Deionized water
RH	Relative Humidity
TEOS	Tetraethyl orthosilicate
XRD	X-Ray Diffraction
ICDD	International Center for Diffraction Data
CV	Cyclic Voltammetry
RT	Room Temperature
EtOH	Ethanol
PREM	Partnership for Research and Education in Materials

ABSTRACT

The first part of this thesis proposes methods to monitor internal corrosion before catastrophic events occur. Internal corrosion accounts for about 60% of all natural gas transmission and gathering pipeline incidents caused by corrosion. In this work, first, nickel, copper, and iron were electrolessly coated on a single mode optical fiber and confirmed by Scanning Electron Microscope (SEM) and X-ray Photoelectron Spectroscopy (XPS). An Optical Backscatter Reflectometer (OBR) was then used to obtain optical measurements during electroless coating of corrosion proxy materials on the fiber, and their dissolution (corrosion). Three types of optical fiber-based sensors are proposed to monitor corrosion and water/humidity in natural gas transmission pipelines.

The second part of this thesis focuses on the study of vanadium sulfide compounds as potential cathode materials for battery applications. Recent theoretical predictions show high magnesium ion mobility in six-coordination, spinel close-packed frameworks. Mg-ion has been reported to favor octahedral environment in sulfides like vanadium sulfides. This project focuses on investigating vanadium sulfide compounds, $A_xV_5S_8$, $A_xV_6S_8$, and V_5S_8 (A = alkali metal or divalent, and x = 0 – 0.8) as candidate cathode materials for Mg-ion battery application.

Stoichiometric mixtures of vanadium sulfide compounds were synthesized in evacuated sealed quartz tubes and handled under argon. As-prepared samples of $A_xV_6S_8$, $A_xV_5S_8$, and V_5S_8 were characterized by powder XRD. The XRD patterns of $Rb_xV_5S_8$,

$Rb_xV_6S_8$, and V_5S_8 matched with ICDD reference patterns without phase impurities. Cyclic voltammetry and chronopotentiometry data of the vanadium sulfide compounds with a lithium anode and the lithium-ion electrolyte suggest that $K_xV_5S_8$ and $Rb_xV_5S_8$ are not electrochemically active. V_5S_8 was found to reversibly intercalate lithium and is a promising electrode material for further study.

1. INTRODUCTION TO ELECTROLESS PLATING

Electroless Plating

This section will discuss the principle and bath composition of electroless plating, and emphasize electroless plating on non-conductive substrates.

1.1 Electroless Plating Principle

Electroless plating is the chemical deposition of a metal on a substrate without applying an external electric current.[1] It starts and proceeds by an electrochemical mechanism involving oxidation (loss of electron) and reduction (gain of electron). As in most electrochemical processes, an electrolyte facilitates the oxidation and reduction reactions between chemical species.[2] Likewise, during electroless plating, a complex aqueous solution of the salt of the metal to be deposited acts as an electrolyte. The presence of a reducing agent in the solution initiates the deposition of the said metal on the surface of a substrate immersed in the solution. The process continues to deposit the metal autocatalytically on the initial metal deposit.[1]

Electroless plating depends on two actions: cathodic (metal deposition) and anodic (oxidation of reductant). These actions rely, first, on the redox potential for the chemical reactions being more positive than the immersed metal substrate.[1,3] Second, on the surface of the substrate having enough catalytic activity to initiate the metal ion reduction.[3] If both conditions are met, then the metal ions will be selectively reduced on the surface of the conductive substrate.

The cathodic and anodic chemical reactions during electroless plating are described in Equations 1 – 2:

Cathodic reaction,

$$MC_m^{n+1} + ne^- \rightarrow M^0 + mC \quad (1)$$

Anodic reaction,

$$Red \rightarrow Ox + ne^- \quad (2)$$

where *M* is the metal, *C* the complexing agent, *Red* the reducing agent, *Ox* the oxidized product, and *n* the number electrons.

Electroless plating occurs in a plating bath consisting mainly of a metal ion source, reducing agent, and a complexing agent. Depending on the type of metal ion source, the components of the plating bath may contain other additives. The composition, thickness, and rate of deposition depend on the factors listed below:[4]

i. The pH of the solution
ii. Concentration of chemical components
iii. Composition of reducing agent
iv. Temperature

1.2 Electroless Plating Bath

The typical electroless plating bath consists of a metal ion source, suitable complexing agent, stabilizer, and reducing agent. Often, pH regulator, inhibitor, and other additives are introduced to improve plating bath and the quality of the deposit.[5]

1.2.1 Metal Ion Source

The metal ion source, usually a salt of the metal to be deposited, supplies the metal ion that is reduced during the plating process. It is beneficial to choose a salt whose anion component does not degrade nor is harmful to the substrate. For example, the chloride in nickel chloride will deteriorate an aluminum substrate.[1] However, nickel sulfate or nickel hypophosphite are less harmful to substrates.[6,7] Copper sulfate and iron sulfate are the preferred salts for electroless copper and iron plating processes respectively.[5,8–10]

1.2.2 Reducing Agent

A reducing agent in a plating bath supplies the electrons to reduce the metal ions in solution. Typically, this reduction results from the dehydrogenation of the reducing agent.[1] Thus, the reductant must contain reactive hydrogens for sufficient reducing power. Typical reducing agents such as sodium hypophosphite, sodium borohydride, dimethylamine borane, hydrazine, formaldehyde have two or more reactive hydrogens. The reductant should also have a more negative redox potential than the metal to be deposited to limit the electrochemical reactions only on the surface of the substrate and prevent homogenous decomposition of the plating bath.[11] If the reductant has a more positive redox potential, it will lead to spontaneous disintegration of the plating bath.

As shown in Table 1, the redox potential of hypophosphite is – 1.57 at pH between 7 and 10, while that of nickel (Ni) is − 0.250. Since the value of the redox potential of hypophosphite is less than that of Ni, Ni will deposit on the substrate only. However, when formaldehyde (HCOOH) which has a redox potential of 0.056 at pH 0, is added to a silver nitrate bath (redox potential of silver is 0.799), the plating bath decomposes, and instantaneous silver metal precipitates out.[1] The reduction of silver-ion to silver-metal occurs in solution instead of the surface of the substrate. So, the choice of reducing agent is vital for the best coating result.

Table 1. Standard Redox Potential at 25º C.[1]

Reaction	**Potential (V vs. SHE)**
$Ag^{+} + e^{-} \leftrightharpoons Ag^{0}$	+ 0.799
$Cu^{2+} + 2e^{-} \leftrightharpoons Cu^{0}$	+ 0.340
$HCOOH + 2H^{+} + 2e^{-} \leftrightharpoons HCHO + H_2O$ (pH = 0)	+ 0.056
$Ni^{2+} + 2e^{-} \leftrightharpoons Ni^{0}$	– 0.250
$Fe^{2+} + 2e^{-} \leftrightharpoons Fe^{0}$	– 0.440
$H_2PO_3^- + 2H^+ + 2e^- \leftrightharpoons H_2PO_2^- + H_2O$ (pH = 4-6)	– 0.499
$B(OH)_4^- + 4H_2O + 8e^- \leftrightharpoons BH_4^- + 8OH^-$ (pH = 12-14)	– 1.24
$H_2PO_3^- + 2H^+ + 2e^- \leftrightharpoons H_2PO_2^- + H_2O$ (pH = 7-10)	– 1.57

Research has shown that reducing agents containing phosphorus (P) and boron, (B) co-deposit these elements, respectively during electroless plating.[4,9,12,13]. An example is the electroless deposition of Ni-P alloy by using sodium hypophosphite as the reducing agent.[14] Or Fe-B alloy using sodium borohydride as the reducing agent.[12]

1.2.3 Complexing Agent

Complexing agents are mainly used to prevent precipitation of the metal salt, buffer the solution pH, and reduce the concentration of free metal ions in solution.[1] They are usually ligands that replace coordinated molecules to the metal ion. The swapping of these coordinated ligands results in a color change and increases the solubility during bath preparation.[1] In electroless nickel plating (ENP) bath preparation, the plating bath changes color from green to blue when six ammonium ligands from the complexing agent replace six water molecules of the nickel sulfate hexahydrate salt,[1] as shown in Equation 3.

$$[Ni(H_2O)_6]^{+2} + 6NH_3 \rightarrow [Ni(NH_3)_6]^{+2} + 6H_2O \quad (3)$$

Green Blue

Notwithstanding the physical impact of the complexing agent during bath preparation, it also affects the deposition rate, composition, morphology, structure, and stability of the plating bath.[4,5,15–18] The rate of deposition of the metal coating increases as complexing agent concentration increase but decreases with subsequent increase in ligand concentration if the solution is pH buffer stable.[16] Sodium citrate dihydrate (Figure 1) was used as a complexing agent for nickel and iron electroless plating while potassium sodium tartrate tetrahydrate (Figure 2) for electroless copper plating (ECP).

1.2.4 pH regulator

A pH regulator is used to adjust the final pH of the plating bath. In electroless nickel plating, sodium hydroxide (NaOH) was used as a pH regulator to change an acidic bath to an alkaline bath. Table 2 lists common pH regulators for electroless Ni and Cu plating.

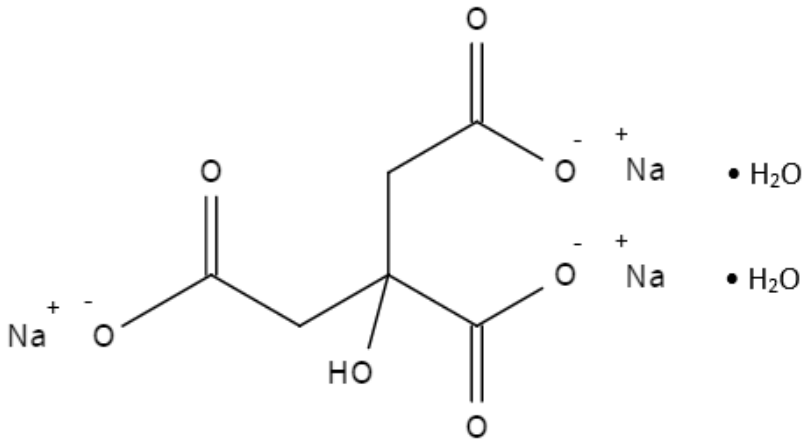

Figure 1. Structure of sodium citrate dihydrate

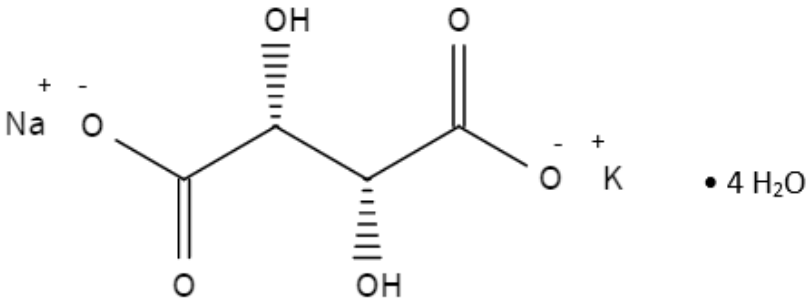

Figure 2. Structure of Potassium sodium tartrate tetrahydrate

1.2.5 Stabilizers

Electroless plating baths are thermodynamically unstable because the concentration of each component in solution varies wildly. Although it is challenging to control bath stability, adding stabilizer to the bath will prevent homogenous reactions that will lead to spontaneous bath decomposition.[19] Stabilizers are sometimes referred to as catalytic inhibitors or anti-catalysts because they inhibit hydrogenation and dehydrogenation catalysts. An effective stabilizer should not hinder catalytic activity and should result in a net improvement of deposit results.

The most commonly used stabilizers are classified into four groups:[1]

1. Compounds of these group IV elements: sulfur, selenium, and tellurium
2. $AsO_2^-, IO_3^-, MoO_4^{2-}$
3. Sn^{2+}, Pb^{2+}, Hg^+, Sb^{3+}
4. Maleic, itaconic – organic acids that are not saturated

Common stabilizers used in electroless nickel and copper plating are in Table 2.

Table 2. Some stabilizers and pH regulators for electroless Ni & Cu bath.[5,20,21]

Electroless plating bath	**Acidic nickel**	**Alkaline nickel**	**Copper**
Stabilizer	Thiourea	Thiourea	Thiourea
	Thioorganic compound	Thioorganic compound	Vanadium pentoxide
	Lead acetate	Lead acetate	Oxygen
	Heavy metal salts	Heavy metal salts	Diethyldithiocarbamate
		Thallium salts	2-mercaptobenzothiazole
pH regulator	Sodium hydroxide	Sodium hydroxide	Sodium hydroxide
	Sulfuric acid	Sulfuric acid	Acetic acid
		Ammonium hydroxide	Ammonia

1.2.6 Energy

The energy required for metal deposition during electroless plating is supplied by temperature in the form of heat.[1] The temperature of the plating bath affects the rate of deposition.[4] Electroless nickel and copper plating requires temperatures above room temperature to proceed while electroless iron plating does not.

1.3 Electroless Plating on a Non-conductive Substrate

The surface of the substrate for electroless plating should either be conductive (metallic) or non-conductive with metal catalysts since a catalytic surface is required. During the plating process on either surface, the first thin film metallic layer deposited acts as a catalyst for subsequent deposits. It is important to note that the substrate should not act as the reducing agent or dissolve during this process.[21] It is therefore essential to choose a less noble metal for a conductive substrate than the metal being deposited or activate the surface of a non-conductive substrate for nucleation to begin.

The surface of a non-conductive substrate is typically coarsened, sensitized and activated with a metal catalyst to begin the plating process.[22] Doing so enhances the adhesion of the metal coating to the substrate. The non-conductive surface is often roughened in high concentrated acidic or basic solution. During sensitization in a tin (II) chloride ($SnCl_2$), Sn^{2+} ions adsorb to the surface of the roughened non-conductive substrate. Then during activation in palladium (II) chloride ($PdCl_2$), Pd^{2+} ions are reduced to Pd^0 and Sn^{2+} is simultaneously oxidized to Sn^{4+}.[23] In the reduction to palladium ion to palladium metal, as shown in Equation 4, the Pd^0 on the surface of the substrate acts as the catalyst to initiate the electroless plating process.

$$Sn^{2+} + Pd^{2+} \rightarrow Sn^{4+} + Pd^0 \quad (4)$$

The process of cleaning, coarsening, sensitization, activation, and plating of a nonconductive substrate is illustrated in Figure 3.

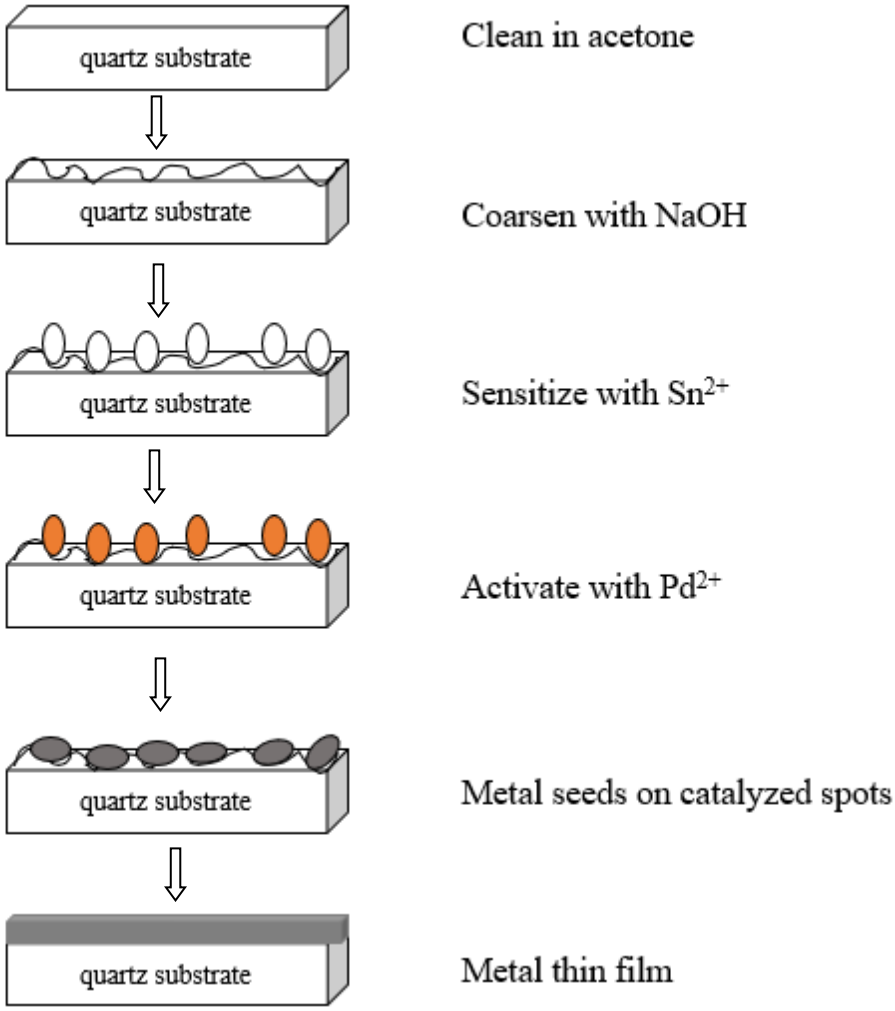

Figure 3. Schematic of sensitization and activation of non-conductive quartz substrate with $SnCl_2$ and $PdCl_2$.[24]

Other methods for fiber pretreatment are: coarsening/etching soda lime glass substrate with nitric acid solution, etching quartz substrates with hydrofluoric acid or a mixture of sulfuric acid and hydrogen peroxide (piranha solution).[25] 3-(2-aminoethyl amino)-propyl-trimethoxy silane (EDA-Si) from a 1 % solution in water has been used to graft a homogenous layer on the surface of glass to bind Pd/Sn solution.[26] Other

researchers have avoided using the sensitization and activation process on glass by first growing copper nanoparticles which act as activators for electroless copper plating.[27] Literature review reveals electroless plating on other non-conductive surfaces like cellulose fibers, wood, and plastic.[10,28,29]

1.4 Electroless Nickel, Copper, and Iron Plating

1.4.1 Electroless Nickel Plating

Electroless nickel plating is by far the more commercially used plating process available. Research has shown that the bath components and conditions determine the composition and thickness of the deposits. It, in turn, determines the physical and chemical properties of the deposited nickel film.[30,31] The typical bath components of ENP is listed in Table 3 below.

Table 3. Components of a typical electroless nickel plating bath.[1,21]

Metal ion source	Reducing agent	Complexing agent	Stabilizer/inhibitor
Nickel sulfate	Sodium hypophosphite	Trisodium citrate	Ammonium chloride
Nickel chloride	Sodium borohydride	Malate	Maleic acid
Nickel hypophosphite	Dimethylamine borane	Ethylenediamine	Itaconic acid
Nickel acetate	Hydrazine	Acetate	Thiourea

The fundamental redox chemical reactions of ENP are listed in Equations 5 – 7. First, the reducing agent is oxidized, and then the nickel ion is reduced to nickel metal as shown below:

Reducing agent (Red) oxidation:

$$Red \rightarrow Ox + 2e^- \quad (5)$$

Nickel ion reduction:

$$Ni^{2+} + 2e^- \rightarrow Ni^0 \quad (6)$$

The net reaction for ENP:

$$Ni^{2+} + Red \rightarrow Ni^0 + Ox \quad (7)$$

But Equations 5 – 7 does not fully represent all the chemical reactions during ENP. For a more comprehensive account, Equations 8 – 16 show the reactions when sodium hypophosphite is used as the reducing agent to deposit a Ni-P alloy:[32,33]

Water is ionized:

$$2H_2O \rightarrow 2H^+ + 2OH^- \quad (8)$$

Hydroxyl ions coordinate to the solvated nickel ions:

$$Ni(H_2O)_6^{2+} + 2OH^- \rightarrow Ni_{(aq)}(OH)_2 + 6H_2O \quad (9)$$

Hypophosphite reacts with the hydrolyzed nickel, and $NiOH^+$ adsorb at the catalytic site:

$$Ni_{(aq)}(OH)_2 + H_2PO_2^- \rightarrow NiOH^+_{adsorbed} + H_2PO_3^- + H^- \quad (10)$$

Adsorbed $NiOH^+$ are reduced to Ni^0 on the surface of the substrate:

$$Ni_{(aq)}(OH)_2 + H_2PO_2^- \rightarrow Ni^0 + H_2PO_3^- + H^+ + OH^- \quad (11)$$

Both hydrogens from Equations 10 and 11 react to give hydrogen gas:

$$H^- + H^+ \rightarrow H_2 \quad (12)$$

The reduced Ni^0 acts as a catalyst and reacts with hypophosphite to co-deposit P:

$$Ni_{cat} + H_2PO_2^- \rightarrow P + NiOH^+_{adsorbed} + OH^- \quad (13)$$

The hydrolyzed nickel after P co-deposition can either react with water or hypophosphite (back to Equation 11):

$$NiOH^{+}_{adsorbed} + H_2O \rightarrow Ni_{(aq)}(OH)_2 + H^{+} \quad (14a)$$

$$NiOH^{+}_{adsorbed} + H_2PO_2^{-} \rightarrow Ni^0 + H_2PO_3^{-} + H \quad (14b)$$

Hypophosphite also reacts with water to give hydrogen gas during the process:

$$H_2PO_2^{-} + H_2O \rightarrow H_2PO_3^{-} + H_2 \quad (15)$$

The overall chemical reaction during ENP:

$$Ni^{2+} + 4H_2PO_2^{-} + H_2O \rightarrow Ni^0 + 3H_2PO_3^{-} + H^{+} + P + 3/2H_2 \quad (16)$$

In the reaction from Equation 10, the constant supply of adsorbed $NiOH^{+}$ on the catalytic surface leads to nickel deposition. Conversely, phosphorus cannot be continuously co-deposited by the reaction in Equation 13 since it produces $NiOH^{+}_{adsorbed}$ that covers the surface of the Ni^0. Metallic Ni surface must be available to react with hypophosphite to co-deposit phosphorus on the substrate. If the adsorbed $NiOH^{+}_{adsorbed}$ reacts with hypophosphite through the reaction in Equation 14b, the catalytic nickel surface is exposed again and free to react with hypophosphite to co-deposit P. $NiOH^{+}_{adsorbed}$ reaction with water in Equation 14a is a competing reaction to its reaction with hypophosphite in Equation 14b. These competing reactions are responsible for the lamellar morphology of ENP[32] which is due to the periodicity of both reactions.

1.4.2 Electroless Copper Plating

The electrochemical process involved in electroless copper plating (ECP) using formaldehyde (HCHO)[1] as a reducing agent is shown in Equations 17 - 19:

Oxidation of reducing agent:

$$2HCHO + 4OH^{-} \rightarrow 2HCOO^{-} + H_2 + 2H_2O + 2e^{-} \quad (17)$$

Reduction of copper:

$$Cu^{2+} + 2e^{-} \rightarrow Cu^0 \quad (18)$$

Overall reaction:

$Cu^{2+} + 2HCHO + 4OH^- \rightarrow Cu^0 + 2HCOO^- + H_2 + 2H_2O$ (19)

Another proposed reaction for ECP using hypophosphite as the reducing agent[34] is shown by reactions in Equations 20 – 22.

Oxidation of reducing agent:

$2H_2PO_2^- + 2OH^- \rightarrow 2H_2PO_3^- + H_2 + 2e^-$ (20)

Reduction of copper:

$Cu^{2+} + 2e^- \rightarrow Cu^0$ (21)

Overall reaction:

$Cu^{2+} + 2H_2PO_2^- + 2OH^- \rightarrow Cu^0 + 2H_2PO_3^- + H_2$ (22)

The typical composition of the electroless copper plating bath is listed in Table 4.

Table 4. Typical components of the electroless copper plating bath.[1,21]

Metal ion source	**Reducing agent**	**Complexing agent**	**Stabilizer**
Copper sulfate	Sodium hypophosphite	Sodium potassium tartrate	Oxygen
Copper chloride	Formaldehyde	Ethylenediamine tetraacetic acid	Thiourea
Copper nitrate	Dimethylamine borane	Glycolic acid	Vanadium pentoxide

1.4.3 Electroless Iron Plating

Electroless iron plating on a non-conductive substrate like glass is less studied than other metals like copper and nickel. A literature search of electroless iron plating on optical fiber was futile at the time of this project. But researchers have reported

successful electroless iron deposition on other non-conductive substrates like cellulose fiber with good adhesion and uniform coating.[10]

The electrochemical process for electroless iron plating bath using sodium borohydride as a reducing agent[1] is proposed to follow reactions in Equations 23 – 28:

Reduction of iron by borohydride:

$$BH_4^- + 4H_2O \rightarrow B(OH)_4^- + 2H_2 + 4H^+ + 4e^- \quad (23)$$

$$2Fe^{2+} + 4e^- \rightarrow 2Fe^0 \quad (24)$$

Overall reaction:

$$BH_4^- + 2Fe^{2+} + 4H_2O \rightarrow 2Fe^0 + B(OH)_4^- + 2H_2 + 4H^+ \quad (25)$$

Reduction of boron which is independent of iron reduction:

$$BH_4^- + H^+ \rightarrow BH_3 + H_2 \rightarrow B^0 + 5/2H_2 \quad (26)$$

Hydrolysis of borohydride:

$$BH_4^- + 4H_2O \rightarrow B(OH)_4^- + 4H + 4H^+ + 4e^- \rightarrow B(OH)_4^- + 4H_2 \quad (27)$$

Overall plating reaction:

$$2Fe^{2+} + 2BH_4^- + 4H_2O \rightarrow 2Fe^0 + B + B(OH)_4^- + 3H^+ + 9/2H_2 \quad (28)$$

Typical composition of an electroless iron plating bath is shown in Table 5 below.

Table 5. Typical components of the electroless iron plating bath.[1,21]

Metal ion source	**Reducing agent**	**Complexing agent**	**Stabilizer**
Iron sulfate	Sodium borohydride	Sodium citrate dihydrate	Boric acid
Ferrous ammonium sulfate	Sodium hypophosphite	Potassium sodium tartrate	
Iron chloride	Hydrazine	Ethylenediamine	

The literature review shows that during electroless iron plating, poor adhesion of Fe deposit to the substrate results from high concentration levels of Fe(II) and BH_4^-.[10] The formation of rust during plating is due to the low concentration of Fe(II) and high pH levels.[10] The pH of electroless iron plating is typically controlled by adding NaOH or ammonia. The temperature of the electroless iron plating bath has been reported to be between 21.5 ºC to 50 ºC.[10,35]

1.5 Reasons for using Electroless Plating

1. Cost-effectiveness: Electroless plating is intrinsically a cheaper process because it does not require an applied external current compared to other methods like electroplating and sputtering.
2. Commercialization: Without the need for applied external current, mass production of metallic-coated fibers by electroless plating makes it easy to commercialize because the process occurs autocatalytically. Moreover, there are several commercial applications of electroless plating in industries like computers, electronics, valves, automotive, and machinery.
3. Relatively fast process: Electroless plating is initiated by adding the reducing agent to the plating bath and metal deposition proceeds autocatalytically until the desired coating is achieved, usually within 2 hours for thin film.
4. Uniform coating thickness: One of the most critical advantages of electroless plating is the quality of the coating, which leads to advantageous physical and mechanical properties. It produces uniform thickness on complicated shapes and geometries.

5. Corrosion resistance: Electroless plating produces a pore-free coating that is resistant to corrosion. Also, since the co-deposition of phosphorus and boron leads to amorphous components of the deposits, the corrosion resistance is high.[21]

2. STATEMENT OF PURPOSE

Corrosion is one of the leading causes of failures in metal transmission pipelines in the US.[36] The Pipeline and Hazardous Materials Safety Administration (PHMSA) reports that from 1998 – 2017, corrosion accounted for about 12 % of all pipeline incidents. According to PHMSA data, it is estimated that internal corrosion accounts for about 60% of incidents in natural gas transmission and gathering pipelines caused by corrosion. It is vital to monitor the structural health of these pipelines before the disastrous impact of corrosion happens. Currently, corrosion in pipelines is mostly monitored by removable coupons placed at locations susceptible to internal corrosion. However, the challenge of distributed corrosion monitoring along the pipeline remains.

Recently, optical fiber-based sensors have sparked renewed interest because of their low cost and immunity to electromagnetic interference. Although researchers have reported on optical fiber-based sensors to detect pH, temperature, gas, humidity, and corrosion,[24,37–41] there are few studies on electrolessly coated optical fiber for distributed corrosion monitoring. In this project, Ni, Cu, and Fe were electrolessly coated on optical fiber and confirmed by SEM and XPS. An optical backscatter reflectometer (OBR) was then used to obtain optical measurements during plating and dissolution of metallic film coated on the fiber for a distributed corrosion monitoring sensor. This report also includes the proof of concept for an optical fiber-based sensor for monitoring water molecules and an optical fiber-based corrosion sensor with Fe/SiO_2 composite sensing layer.

Distributed Optical Fiber-Based Sensor

Early onset of corrosion can be monitored by incorporating corrosion proxy material on the optical fiber sensing platform to give insight on internal corrosion in pipelines. Figure 4 is a schematic of an optical fiber-based sensing platform. The red arrows present the backscattered light at the discontinuities along the core of a single mode (SM) optical fiber (Figure 6) enabling spatially distributed monitoring using an OBR. The green highlighted region is the gauge length, which can be considered as a sensing data-point.

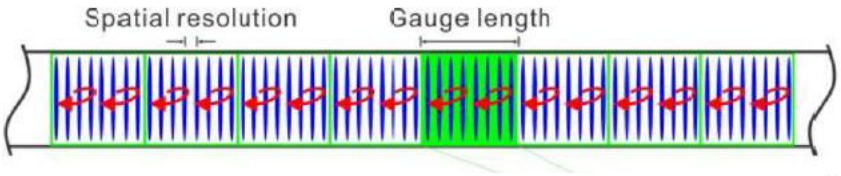

Figure 4. Schematic of the optical fiber-based sensor platform.[42]

Figure 5 shows the corrosion sensing region along the SM optical fiber coated with metallic thin film. As corrosion occurs, the metallic film gets thinner, and then the corresponding optical responses can be detected using an OBR or an optical spectrometer.

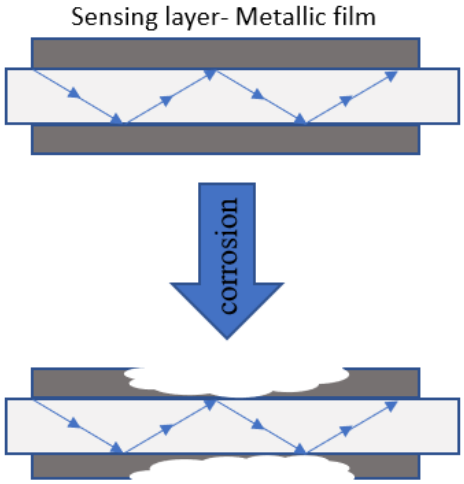

Figure 5. Sensing layer used to monitor the corrosion through optical measurements

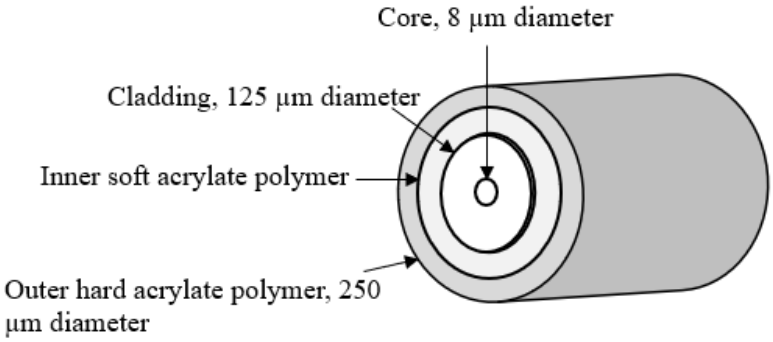

Figure 6. Schematic of dual acrylate coated single mode optical fiber

The OBR (Figure 7) was used to obtain strain-induced optical responses during electroless deposition and subsequent dissolution of the metallic film. The strain changes measured by the OBR is used as a sensing signal to detect and monitor the onset of internal corrosion in pipelines. In distributed sensing, the OBR senses the spectral shift of Rayleigh scattering in the fiber core and makes a distributed strain or temperature measurement.[43] The OBR measurement technique for strain or temperature sensing involves, first measuring the Rayleigh scatter signatures at ambient conditions, and storing it as the shift reference. Then the subsequent scatter profiles are measured when

strain or temperature change is applied along the fiber and cross-correlated to the shift reference taken at ambient conditions. Any shift in the spectrum of the two correlated data is due to strain or temperature[43] along the location on the fiber where the strain or temperature is applied.

Figure 7. Photo of OBR used to interrogate the sensing layer

3. EXPERIMENTAL PROCEDURE

3.1 Pretreatment

The following section discusses the cleaning, coarsening, sensitizing, and activation of a non-conductive substrate for electroless plating.

Cleaning

The protective polymer jacket on the SM optical fiber (SMF28ULTRA, Fiber Instrument Sales, Inc.) was removed with strippers to prepare fibers without a polymer jacket. Isopropyl alcohol was used to remove any residual polymer on the stripped region. The fibers without and with polymer jacket were cleaned by sonicating in acetone for less than 5 minutes and allowed to air dry.

Coarsening

Coarsening increases surface roughness, contact area, and hydrophilicity. The fibers were coarsened in a 400 g/L sodium hydroxide solution (NaOH pellets, Sigma-Aldrich) for 30 minutes at 40 ^{o}C. Then washed by sonicating in distilled water for 5 minutes and dried under a stream of nitrogen.

Sensitization

The fibers were sensitized in a solution consisting of 22.6 g/L tin(II) chloride ($SnCl_2$, 98%, Sigma-Aldrich) and 10.0 mL/L hydrochloric acid (HCl, concentrated) for 20 minutes at 50 ^{o}C. Then rinsed in distilled water and dried under nitrogen.

Activation

The sensitized fibers were activated by immersing them in a solution consisting of 0.795 g/L of palladium (II) chloride ($PdCl_2$, 99%, Aldrich) and 5.00 mL/L HCl for 20 minutes at 50 ^{o}C. They were then rinsed in distilled water and dried under nitrogen.

The two pretreatment methods reported here are shown in Table 6.

Table 6. Two methods of pretreatment of single mode optical fiber before coating

Method A	**Method B**
Sonicate for 15 minutes in acetone	Sonicate for 5 minutes in acetone
Immerse in 10M NaOH for 1 hour at 45 ^{o}C	Immerse in 10M NaOH for 1 hour at 45 ^{o}C
Sonicate for 15 minutes in D.I. H_2O	Sonicate for 15 minutes in D.I. H_2O
Immerse in $SnCl_2$ solution for 20 minutes at 45 ^{o}C	Immerse in $SnCl_2$ solution for 20 minutes at 45 ^{o}C
Immerse in $PdCl_2$ solution for 20 minutes at 45 ^{o}C	Rinse in D.I. H_2O, dry with a stream of N_2
	Immerse in $PdCl_2$ solution for 20 minutes at 45 ^{o}C
	Rinse in DI H_2O, dry with a stream of N_2

3.2 Electroless Plating on SM Optical Fiber

All the chemicals were ACS reagent grade or equivalent. Iron(II) sulfate heptahydrate ($FeSO_4 \cdot 7H_2O$, ≥ 99 %, Sigma-Aldrich), copper(II) sulfate pentahydrate ($CuSO_4 \cdot 5H_2O$, ≥ 98 %, Sigma-Aldrich), nickelous sulfate ($NiSO_4 \cdot 6H_2O$, General Chemical Company), trisodium citrate dihydrate ($C_6H_5Na_3O_7 \cdot 2H_2O$, USP, Sigma-Aldrich), sodium hypophosphite monohydrate ($NaH_2PO_2 \cdot H_2O$, ≥ 99%, Aldrich), ammonium chloride (NH_4Cl, ≥ 99%, Sigma-Aldrich), sodium borohydride ($NaBH_4$, 98 %, Aldrich), boric acid (H_3BO_3, ISO, Merck Millipore), potassium sodium tartrate tetrahydrate ($C_4H_4KNaO_6 \cdot 4H_2O$, 99 %, Sigma-Aldrich).

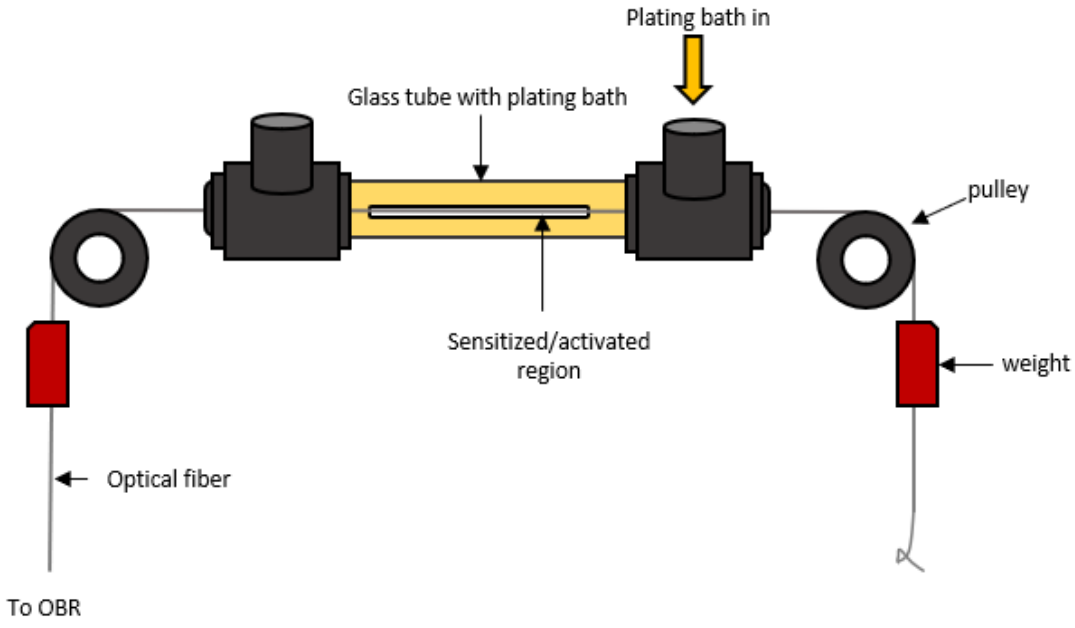

Figure 8. Schematic of the experimental setup for electroless plating on single mode optical fiber

For nickel and iron electroless plating baths, the source of metal ions and the metal chelator were first dissolved in distilled water with stirring. A weighed amount of the pH stabilizer was dissolved in the solution with stirring. The reducing agent solution

was prepared separately by dissolving the reducing agent in distilled water before adding in the plating bath with stirring. The pH and temperature of the plating bath were measured with a pH meter, and the final pH was adjusted with 1.2 M NaOH. For copper electroless plating bath, a solution of the source of metal ions and the metal chelator were first prepared, before the reducing agent was dissolved in the plating solution with stirring. The final, pH was adjusted by adding 1.2 M NaOH to the bath. The detailed electroless plating bath compositions for Ni, Cu, and Fe on SM optical fiber are listed in Table 7.

Table 7. Electroless plating bath composition and conditions for nickel, iron, and copper.

Plating baths	**Ni**	**Fe**	**Cu**
Metal source	19 g/L $NiSO_4 \cdot 6H_2O$	11 g/L $FeSO_4 \cdot 7H_2O$	25 g/L $CuSO_4 \cdot 5H_2O$
Complexing agent	8 g/L $C_6H_5Na_3O_7 \cdot 2H_2O$	57 g/L $C_6H_5Na_3O_7 \cdot 2H_2O$	90 g/L $C_4H_4KNaO_6 \cdot 4H_2O$
Reducing agent	15 g/L $NaH_2PO_2 \cdot H_2O$	3.0 g/L $NaBH_4$	40 g/L $NaH_2PO_2 \cdot H_2O$
pH stabilizer	6.5 g/L NH_4Cl	10 g/L H_3BO_3	
pH at temperature	5 @ 45 ^oC	9.8 @ 22.5 ^oC	8.1 @ 40.5 ^oC
Solution temp.	45 ^oC	22.5 ^oC	40.5 ^oC
Plating rate	16 nm min^{-1}	5.5 nm min^{-1}	4 nm min^{-1}

3.3 OBR Measurement

The fiber was placed in a quartz tube (about 30 cm) with the sensitized and activated region of the fiber at the center of the tube. The fiber directly outside each end of the tube was hung around to a pulley (about 40 cm from one pulley to the other pulley). Weights of the same mass were attached to the fiber after each pulley so that the fiber goes through the hanging attached weights. The weights kept the fiber in the quartz tube straight and evenly distributes any microstrain. The left end of the fiber was attached to the OBR (LUNA, OBR 4600). A knot was tied at the right end of the fiber to stop light propagation and mitigate the light reflection at the fiber tip. The quartz tube was preheated to the desired temperature for high-temperature plating baths. For the microstrain measurements, references were taken before strain measurements to show the effects of the weights and solution addition. When the solution was poured into the glass tube, a new microstrain measurement was taken and set as the solution reference, and then microstrain measurements were taken at different time intervals after that to record the strain changed solely due to electroless plating. Similarly to the dissolution/corrosion tests.

4. RESULTS OF ELECTROLESS PLATING

4.1 Electroless Plating on SM Optical Fiber

4.1.1 Pretreatment

Two methods of pretreatment were compared to improve adhesion and coating quality, as listed in Table 6. In pretreatment method A, mechanical damage to the polymer jacket on the SM optical fiber substrate was observed. The dual acrylate polymer jacket was detached from the cladding of the SM optical fiber after sonicating in acetone for 15 minutes. However, when the SM optical fiber was sonicated for less than 5 minutes, no mechanical damage was observed on the polymer jacket. Sonicating the SM optical fiber in acetone for 15 minutes, mechanically damaged the dual polymer jacket and caused the polymer to lose adhesion to the cladding of the fiber. Also, when the pretreatment involved quick rinsing after sensitization and after activation, then drying under nitrogen, the coating and adhesion improved. An SEM image of the fiber coated with nickel, with this pretreatment shows a uniform nickel coating (Figure 9).

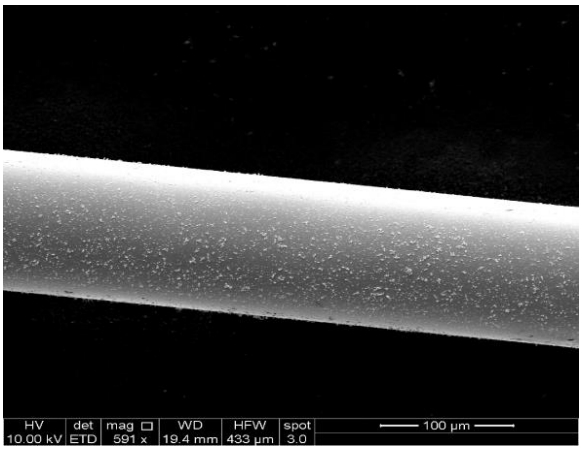

Figure 9. SEM image on the surface of uniform electrolessly nickel coated SM optical fiber with rinsing.

4.1.2 Electroless Nickel Plating

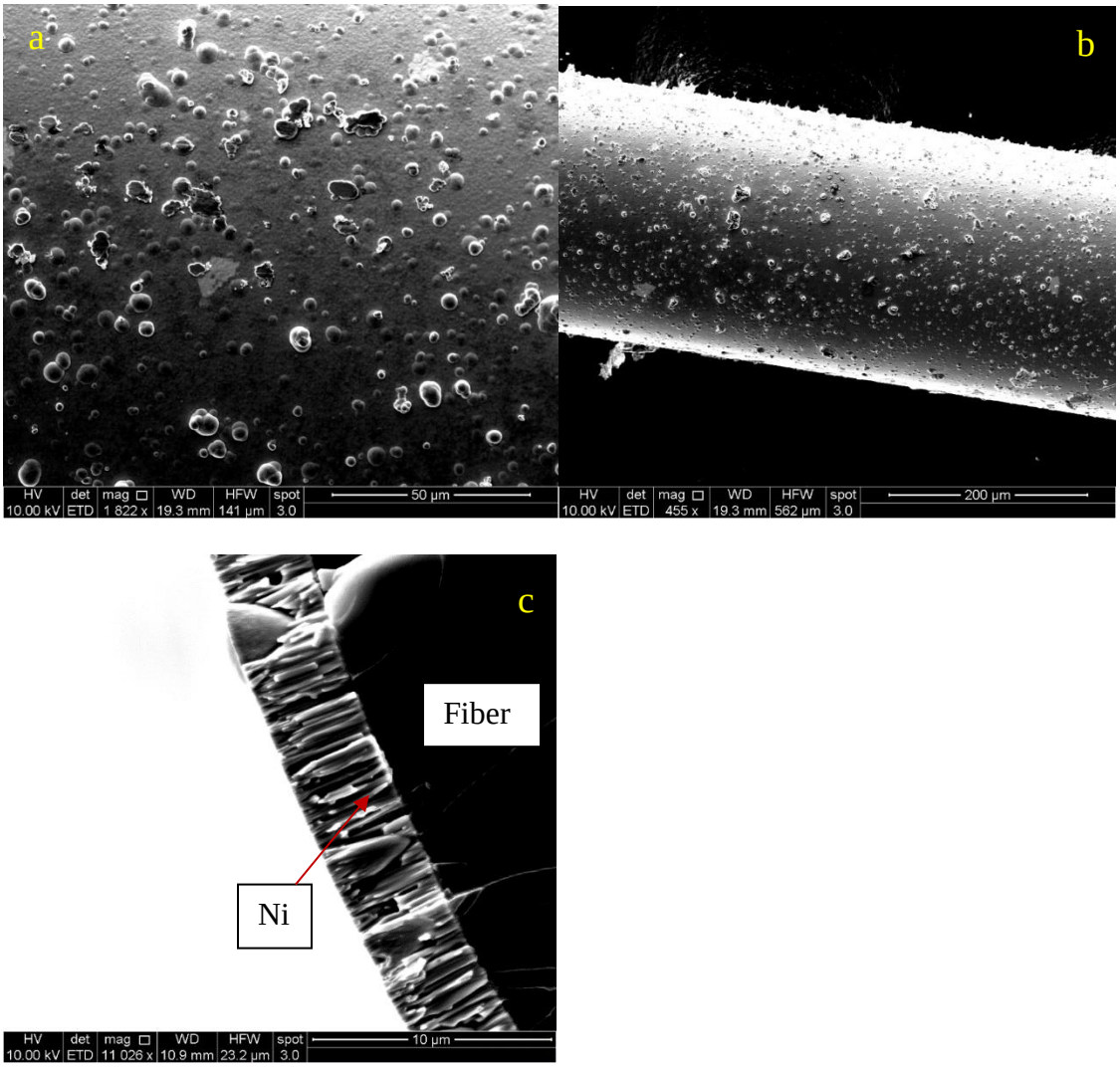

Figure 10. SEM images of the surface of electrolessly coated Ni film on SM optical fiber at the scale of (a) 50 µm and (b) 200 µm showing uniform coating, and (c) SEM image on the cross-section of Ni film showing axial growth.

SEM images confirm that nickel film was coated successfully on the SM optical fiber with polymer jacket (Figure 10). The Ni coating was uniform, as seen in Figure 10b. The SEM on the cross-section shows the Ni film grew in the axial direction with a column morphology, as shown in Figure 10c.

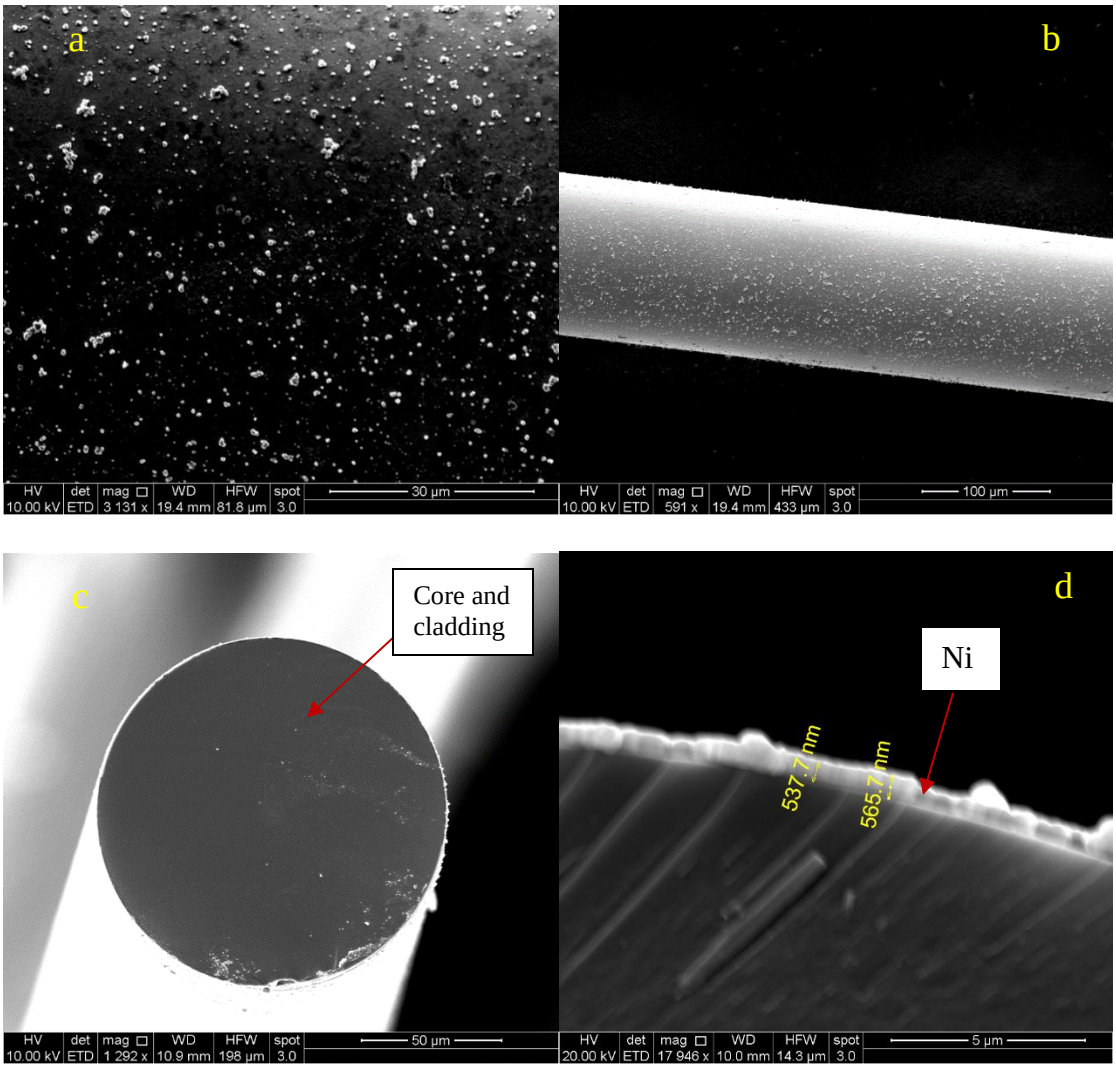

Figure 11. SEM images on the surface of Ni film electrolessly coated on SM optical fiber without polymer jacket at the scale of (a) 30 µm and (b) 100 µm showing uniform coating. SEM images on the cross-section of the same fiber (c) showing the core and cladding at the center without the jacket (d) showing the Ni thin film.

SEM images verify that nickel was also successfully coated on the cladding of SM optical fiber without polymer jacket, as shown in Figure 11. The SEM image of the cross-section shows a much thinner nickel coating.

4.1.3 Electroless Copper Plating

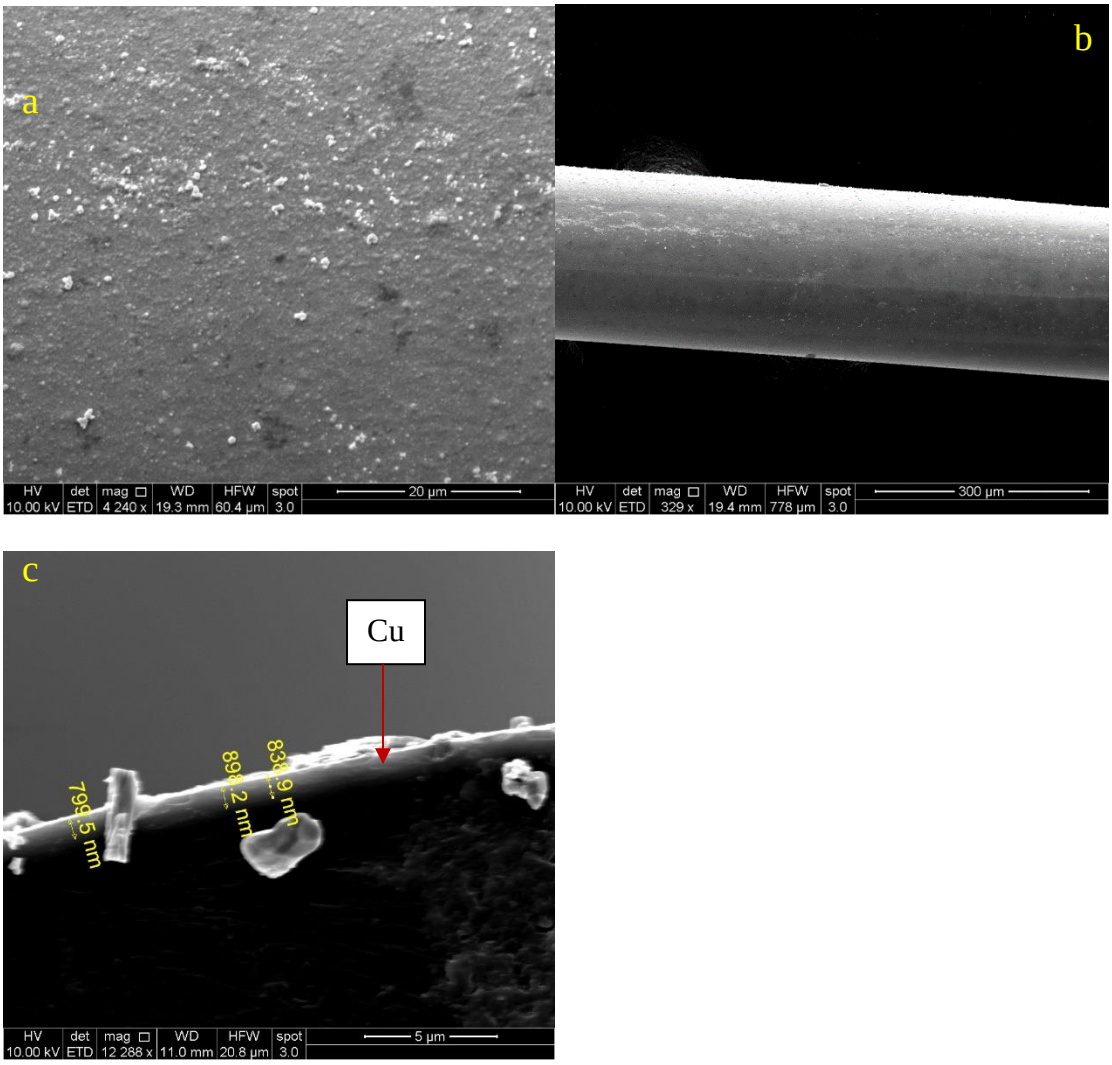

Figure 12. SEM images of the surface of Cu film-coated SM optical fiber by electroless plating at scale (a) 20 µm and (b) 300 µm showing uniform coating. (c) SEM images on the cross-section of the same fiber showing the Cu thin film.

SEM images show that copper film was successfully coated on an SM optical fiber with polymer jacket by electroless plating (Figure 12). The SEM image of the cross-section shows a layer of Cu film.

4.1.4 Electroless Iron Plating

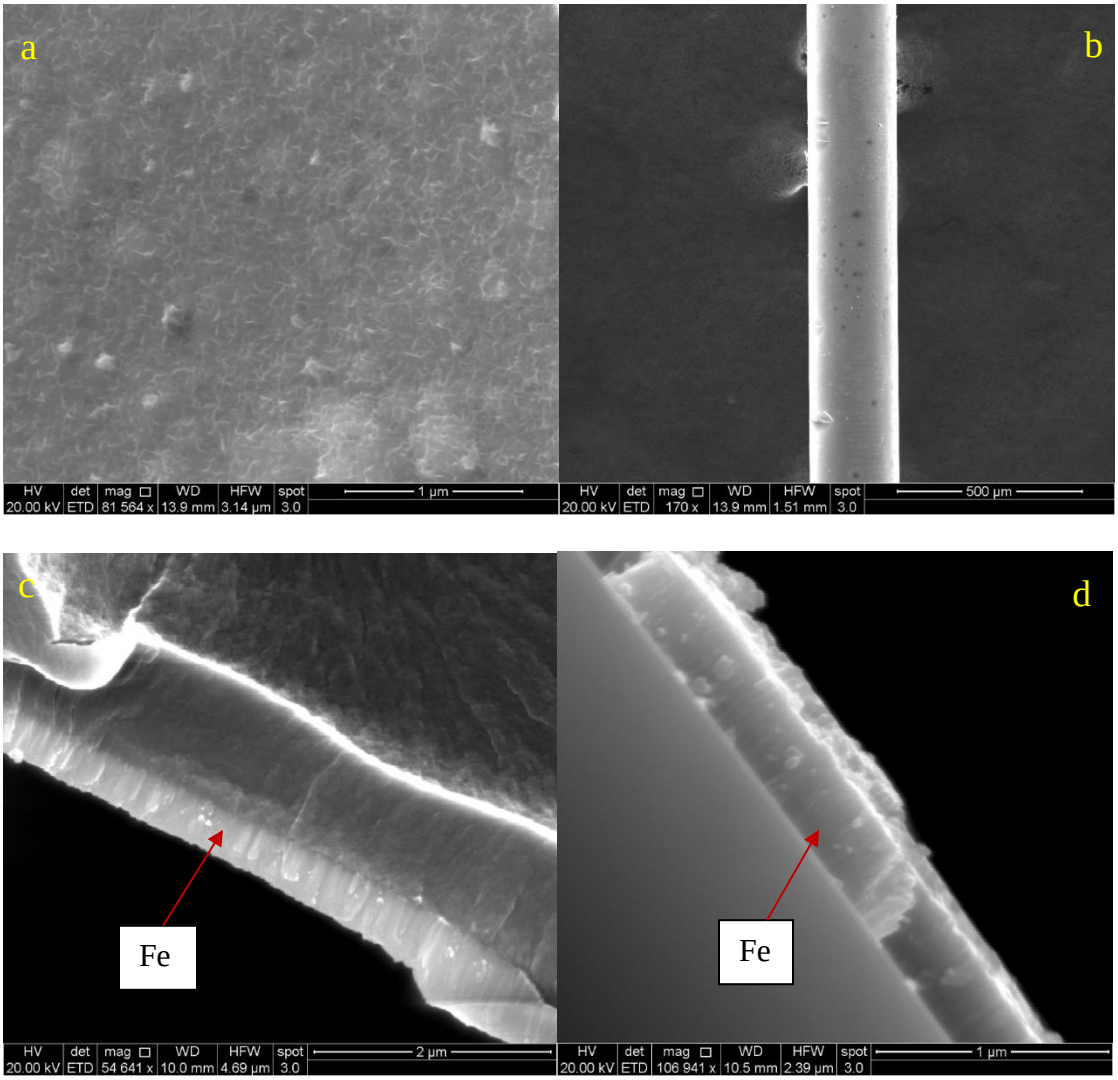

Figure 13. SEM images of the surface of Fe film coated SM optical fiber by electroless plating at scale (a) 1 µm and (b) 500 µm. SEM images on the cross-section of electrolessly coated Fe film on SM optical fiber (a) with and (b) without polymer jacket.

SEM images, as shown in Figure 13, confirms that Fe film was successfully coated on the SM optical fiber with and without polymer jacket by electroless plating. The Fe deposits grew in the axial column direction, as shown in Figure 13 c and d.

Overall, SEM images confirmed that Ni, Cu, and Fe films were uniformly coated on SM optical fibers. On SM optical fibers with polymer jacket, electroless Ni plating had the fastest plating rate, 16 nm min^{-1}, Fe plating had a rate of 5.5 nm min^{-1}, and copper plating was the slowest at 4 nm min^{-1}. Without the polymer jacket, Fe coated at about the same rate of 5.1 nm min^{-1}, and Ni coated at 5 nm min^{-1}.

4.2 Electroless Iron Plating on 5-meter Long SM Optical Fiber

The application design for an electrolessly coated optical fibers for distributed corrosion monitoring requires the coating of an extended length of SM optical fiber. Five meters of SM optical fiber was coiled on a holder, as shown in Figure 14, and immersed in a Fe electroless plating bath. Within one hour at room at 21.5 ^{o}C, the entire length immersed in solution was uniformly coated with Fe film, as shown in Figure 14. This demonstrates the ease at which mass production of electrolessly coated Fe SM optical fiber can be achieved.

Figure 14. Fe film electrolessly plated on 5 meters of SM optical fiber

4.3 X-Ray Photoelectron Spectroscopy (XPS)

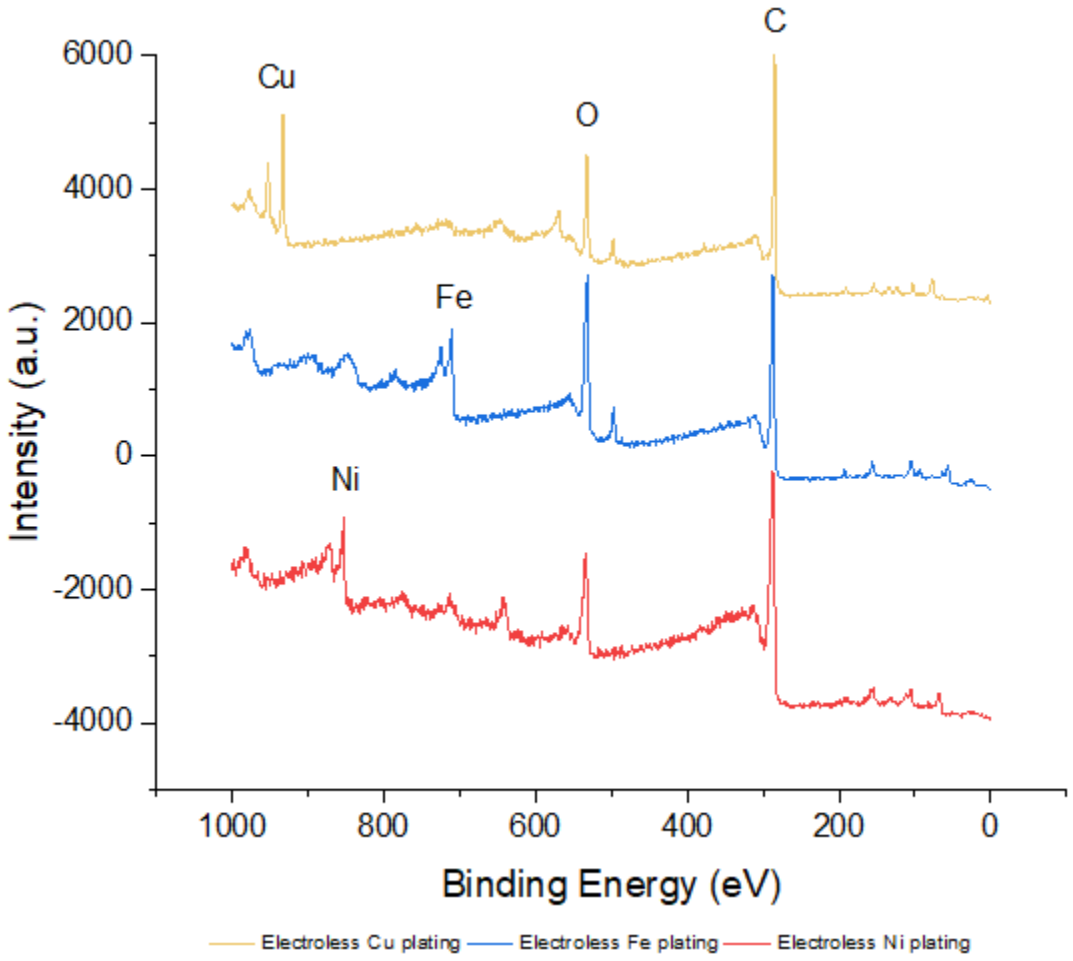

Figure 15. XPS spectrum of Cu, Ni, and Fe films coated on SM optical fibers by electroless plating.

As shown in Figure 15, the XPS spectrum analysis indicates the chemical composition of Ni, Cu, and Fe film on the electrolessly coated SM optical fibers. The carbon and oxygen content were also identified due to adventitious carbon and top-surface oxidation.

5. ELECTROLESSLY COATED OPTICAL FIBERS FOR DISTRIBUTED CORROSION MONITORING

The distributed sensing measurements of the OBR provides a spatial profile of microstrains along the optical fiber with low spatial resolution. Strain changes due to applied strain or temperature during plating and dissolution events on the fiber can be monitored by this method. The SM fiber with the activated and inactivated region was stabilized in the glass tube (Figure 16) to get a reference strain measurement.

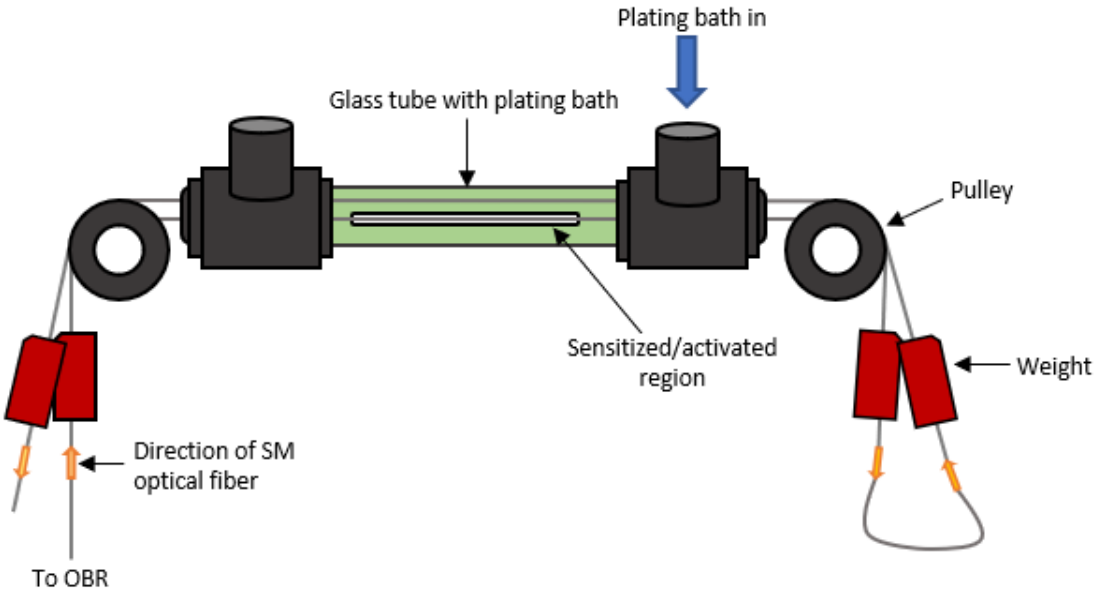

Figure 16. Schematic of setup for two regions of fiber in glass tube.

Weights of the same size were attached at the four ends of the fiber hanging on the pulley (Figure 16) to stabilize the fiber. The weights induced positive microstrain on both the activated and inactivated region of the fiber, as shown in Figure 17, and the strain measurement was set as the reference. The glass tube containing the fiber was preheated for 30 mins to the desired plating temperature of 45 ^{o}C which induced about

450 microstrain over 20 minutes (Figure 18). The microstrain measurement due to preheating was set as a new shift reference for subsequent measurements.

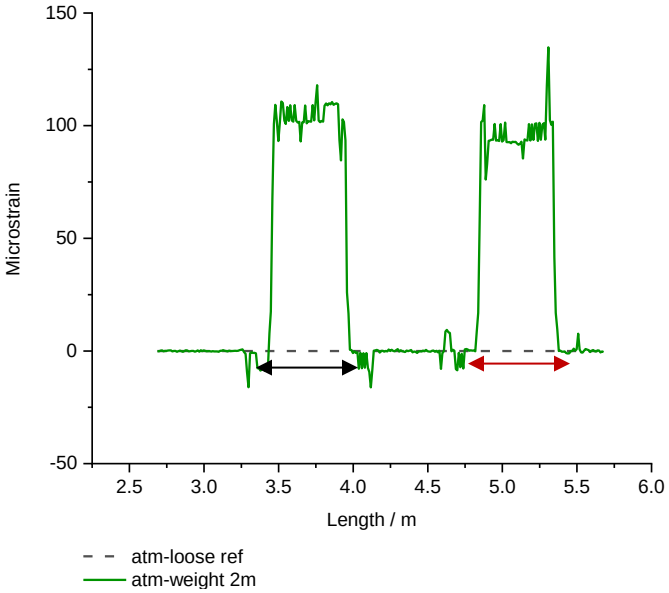

Figure 17. Attached weights induced positive microstrains on the activated (black arrow) and inactivated (red arrow) along the SM optical fiber.

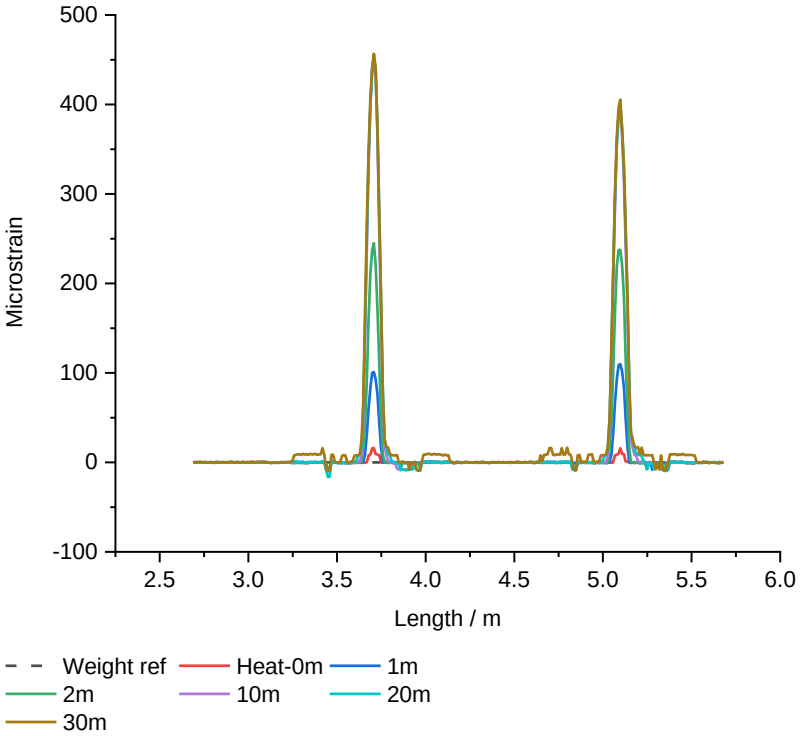

Figure 18. Preheating the glass tube containing the activated and inactive region of the fiber induced positive microstrain which grew over time.

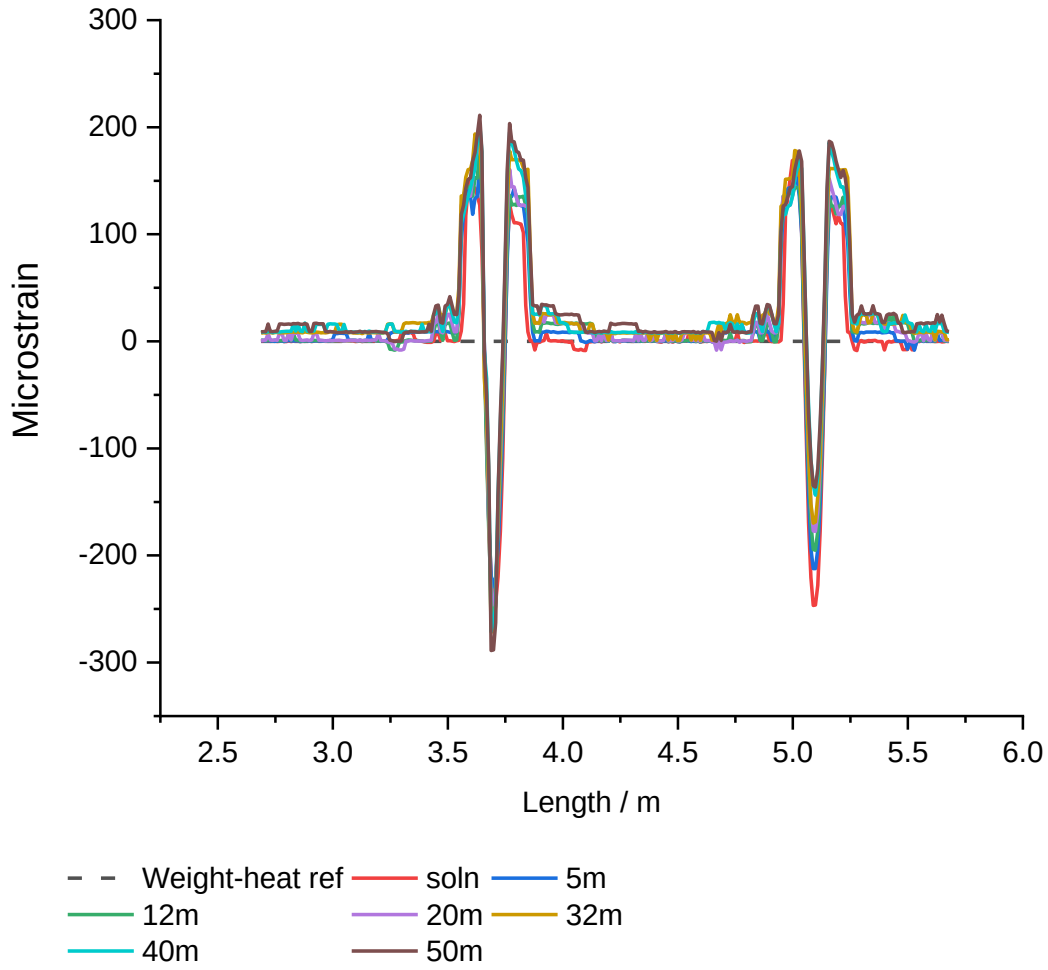

Figure 19. The plating solution induced negative microstrain on both the activated region (left response) and the inactivated (right response). Electroless Ni deposition induced increasingly more negative microstrain on the activated region (coated) only.

The plating bath was poured into the glass tube (in Figure 16) containing the preheated fiber with the weights attached, and microstrain measurements were taken over time. When the solution was poured, both the activated and inactivated regions of the fiber induced positive microstrain and a -250 microstrains drop in the middle of each region of interest on the fiber (Figure 19). The drop (negative microstrain) is due to the temperature change between the preheated fiber and the plating bath. While the induced

positive microstrain is due to the aqueous plating bath, a new reference was not set at this stage because any microstrain change on the treated region will be due to the induced strain from electroless plating and temperature while the untreated region will be due to temperature change only. The difference in microstrains between the activated and inactivated regions of the fiber will give the net microstrain change due to electroless plating only. As nickel deposited electrolessly on the treated region, the microstrain grew more negative over time, while the untreated region grew more positive microstrain over time.

The plot of the maxima of each microstrain measurement taken at a specific time for both the activated and inactivated regions of fiber show two opposing trends (Figure 20). The solution was poured at time = 0, and after about 5 minutes (enough time for electroless plating process to initiate and proceed), the activated region of the fiber grew more negative microstrain while the inactivated region grew more positive microstrain over time (Figure 20). After 50 minutes of plating, the difference between the induced microstrain values on the activated and inactivated region was about 153 microstrains. This value is due to strain change induced by nickel deposition only. This demonstrates that Ni deposition can be monitored at a specific location along an SM optical fiber.

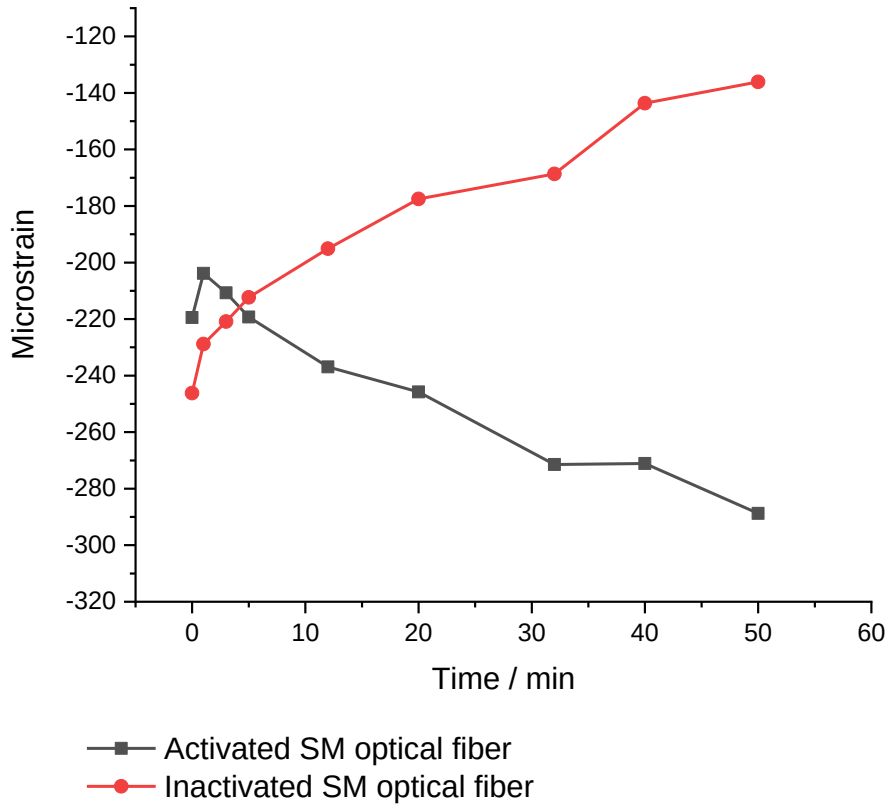

Figure 20. Electroless Ni plating induced more negative microstrain over time on the activate region (black plot) of the fiber, while the microstrain in the inactivated region (red plot) grew more positive over time. Net strain induced by ENP after 50 minutes was 153 microstrain.

As reported in an earlier publication, during the dissolution of electrolessly coated nickel film in an HCl solution of pH 0, the dissolution induced positive microstrain over time.[44] As shown in Figure 21, when electrolessly Ni coated SM optical fiber is exposed to HCl solution of pH 0, as the nickel dissolves it induces positive microstrains on the region with the coating only (red arrow in Figure 21). This demonstrates distributed sensing of corrosion onset and location on nickel coated SM optical fiber.

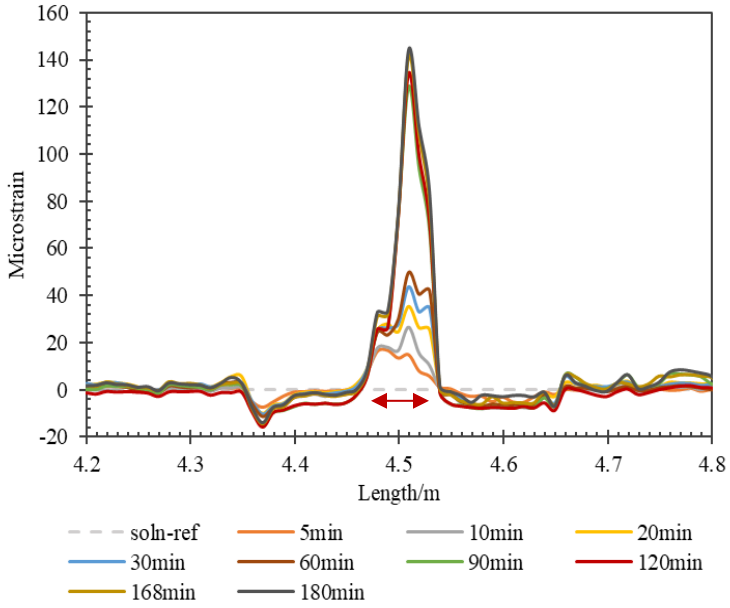

Figure 21. Positive microstrain was induced during Ni film dissolution in 1M HCl solution.[44]

An untreated SM optical fiber exposed to an aqueous solution of either the plating bath or HCl solution showed an induced positive microstrain (Figure 19). The effect of DI water on the untreated SM fiber was investigated to understand its impact. This is of interest because water detection has been used to monitor internal corrosion in gas pipelines.[45] DI water induced positive microstrain on an untreated SM optical fiber, as shown in Figure 22. This is due to the hygroscopic dual-layer polymer jacket of the fiber expanding when it absorbs water, causing strain changes on the fiber. The intrinsic polymer jacket can be used as the sensing layer for the OBR to make a fully distributed water monitoring sensor.

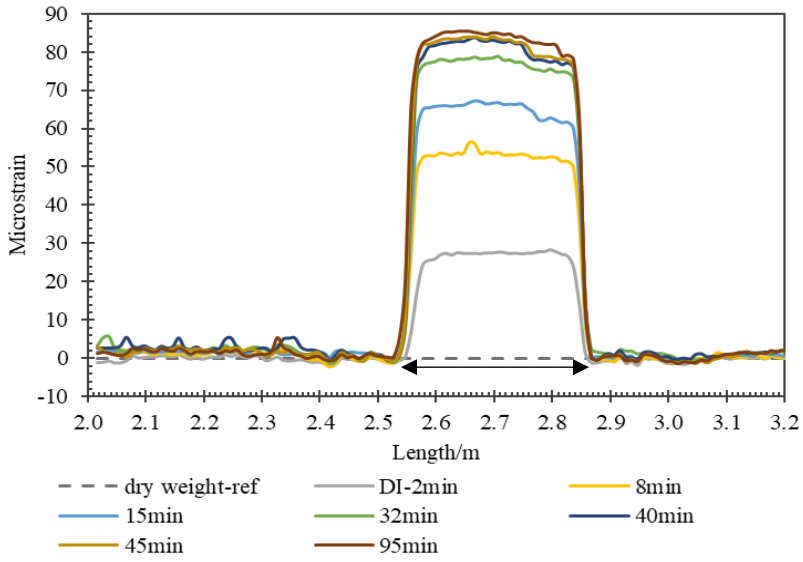

Figure 22. DI water induced positive microstrains on untreated SM optical fiber with dual-layer acrylate polymer jacket (black arrow indicates region exposed to DI water).[44]

6. FULLY DISTRIBUTED OPTICAL FIBER SENSOR FOR WATER AND HUMIDITY MONITORING

In Figure 22, it was observed that DI water induced positive microstrain on untreated off-the-shelf SM optical fiber with hygroscopic dual-layer polymer jacket. Therefore, an untreated SM optical fiber can be used in distributed water detection sensor application. This is important because water acts as an electrolyte to initiate internal corrosion in natural gas transmission pipeline. Since this project focuses on monitoring corrosion, the efficiency of detecting water vapors was investigated and reported below.

The response of the SM fiber to detect water was determined by exposing the fiber to different levels of humidity. Relative humidity (RH) is the amount of water vapor present in the air divided by the amount at saturation point at a given temperature.

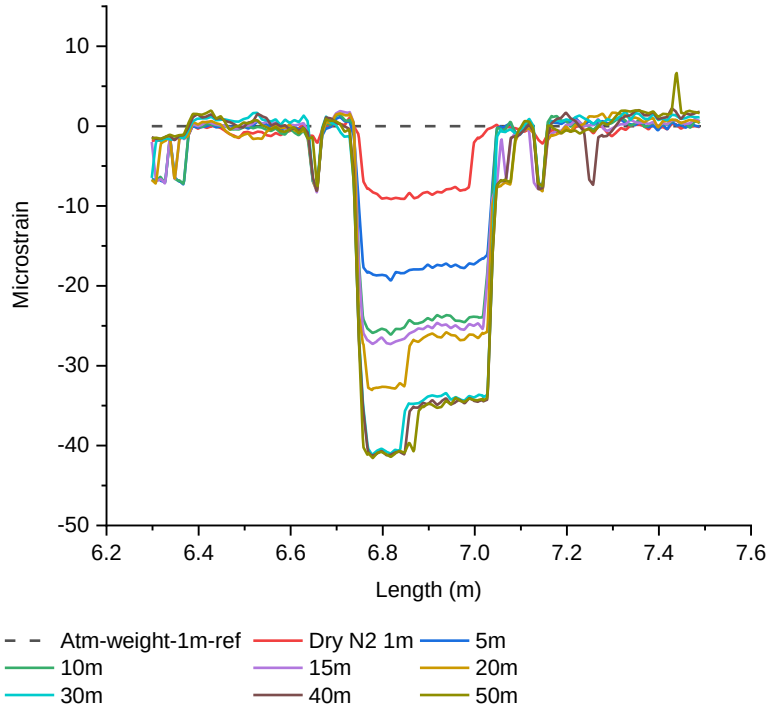

Figure 23. Dry N_2 induced negative microstrain as the off the shelf SM optical fiber was dried; the black arrow is the region of fiber exposed to nitrogen.

First, the untreated of-the-shelf SM optical fiber with dual-layer polymeric covering was installed in the glass tube, and a strain reference was set. Flowing dry N_2 induced negative microstrain on the SM optical fiber over time, as shown in Figure 23. This demonstrates that the polymer jacket on the SM fiber absorbed water from the atmosphere. Therefore, before exposing the fiber to a different RH, the SM fiber was dried first for calibration.

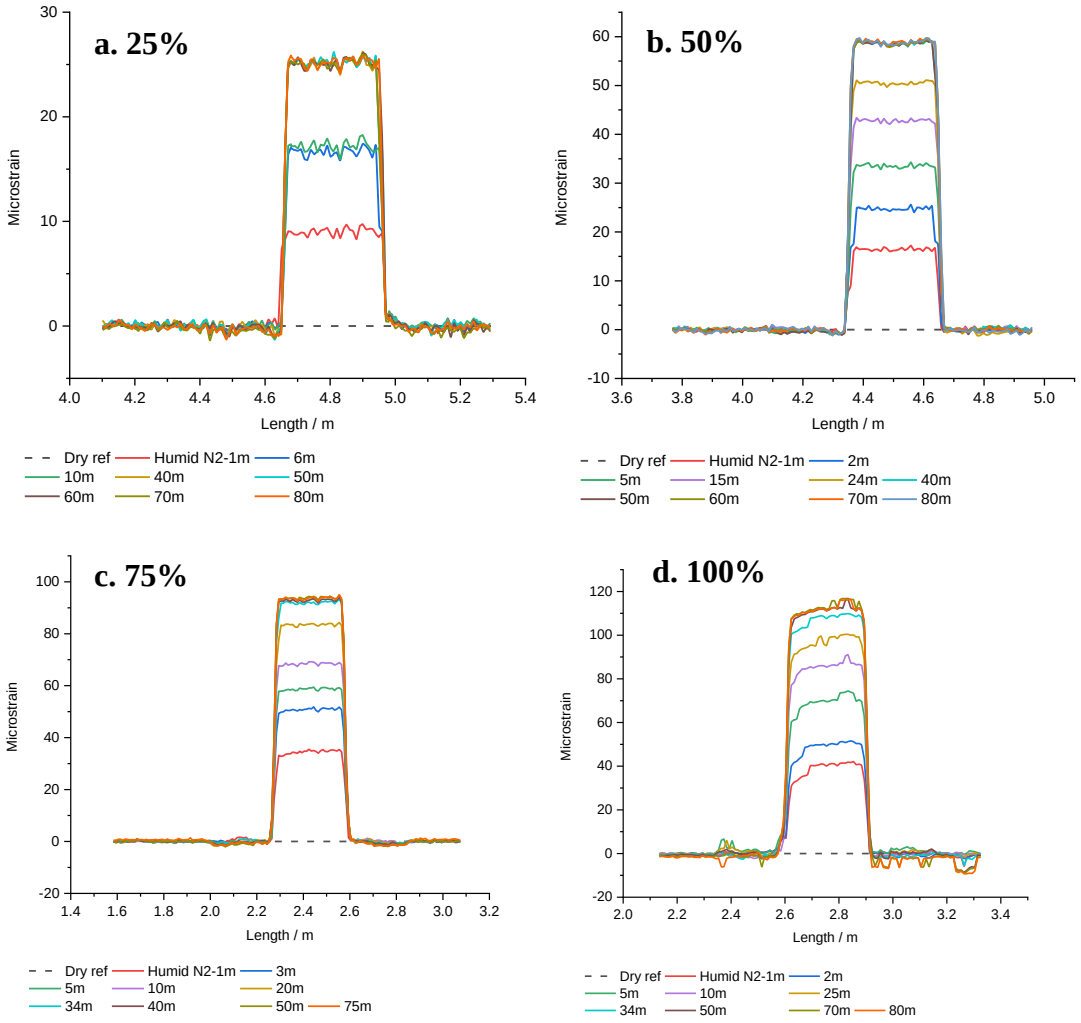

Figure 24. Strain changes along SM optical fiber responding to (a) 25% RH (b) 50% RH (c) 75% RH (d) 100% RH

The strain change due to different RH levels was measured for correlation and reversibility between RH and strain change on the SM fiber. The desired percent RH was introduced by flowing 25, 50, 75, and 100 mL/min wet N_2 from a water bubbler at room temperature and the corresponding dry N_2 flow rate to introduce a total of 100 mL/min flow for each RH level. As shown in Figure 24, the microstrain change due to each %RH stabilized after 50 min, and the strain change responded quickly within 3 minutes until it progressively reached the stable value. In Figure 25, the calibration plot of strain response to different relative humidity levels establishes a linear relationship.

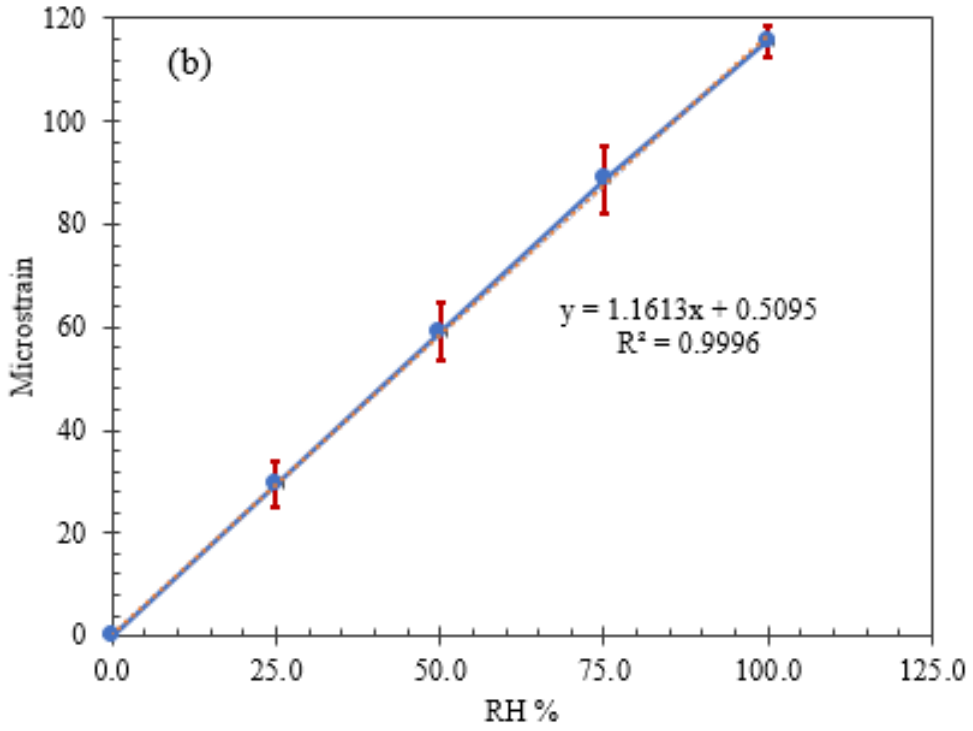

Figure 25. Correlation plot of strain responses at different RH showing a linear relationship.[45]

The reversibility of the humidity sensing of the polymer jacket on the SM optical fiber was tested by cycling between different relative humidity levels and dry N_2 (Figure A7 – A10 in the Appendix). In Figure 26, the plot of strain change at each different RH

level over time, confirms the reversibility of the sensing layer. Although researchers have reported strain response due to humidity using acrylate coated SM fiber,[46] the values from this project are one order of magnitude higher than reported. The linear correlation and reversibility of the strain response at different RH over time and ability to detect the water location along the fiber demonstrate a fully distributed sensor for water and humidity monitoring.

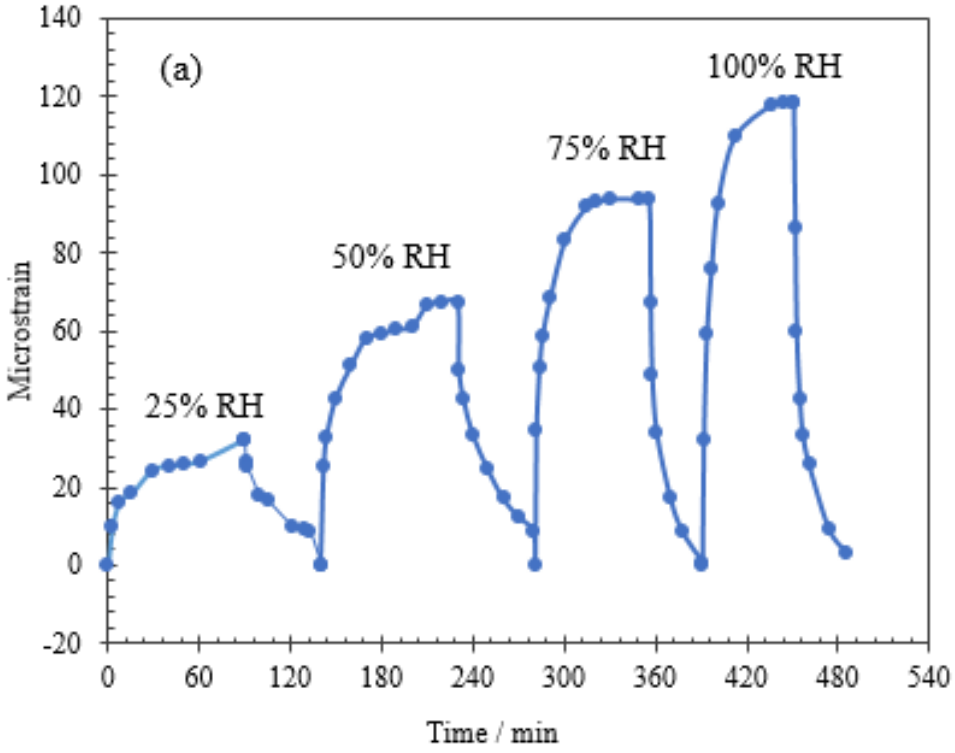

Figure 26. Strain changes over time along the same fiber by cycling at different relative humidity levels.[45]

Although, the distributive sensing of the OBR does not intrinsically differentiate between strain and temperature and since temperature plays a role in relative humidity, the role of temperature was examined. The SM fiber with the dual-layer polymer jacket layer was placed in the glass tube, as shown in Figure 16. A region of the fiber was stripped of the polymer jacket (between the "6.0 – 6.5-meter" mark in Figure 27) to

determine the effect of temperature. The fiber was stabilized with weights of about the same size, and a microstrain measurement was taken and set as the reference.

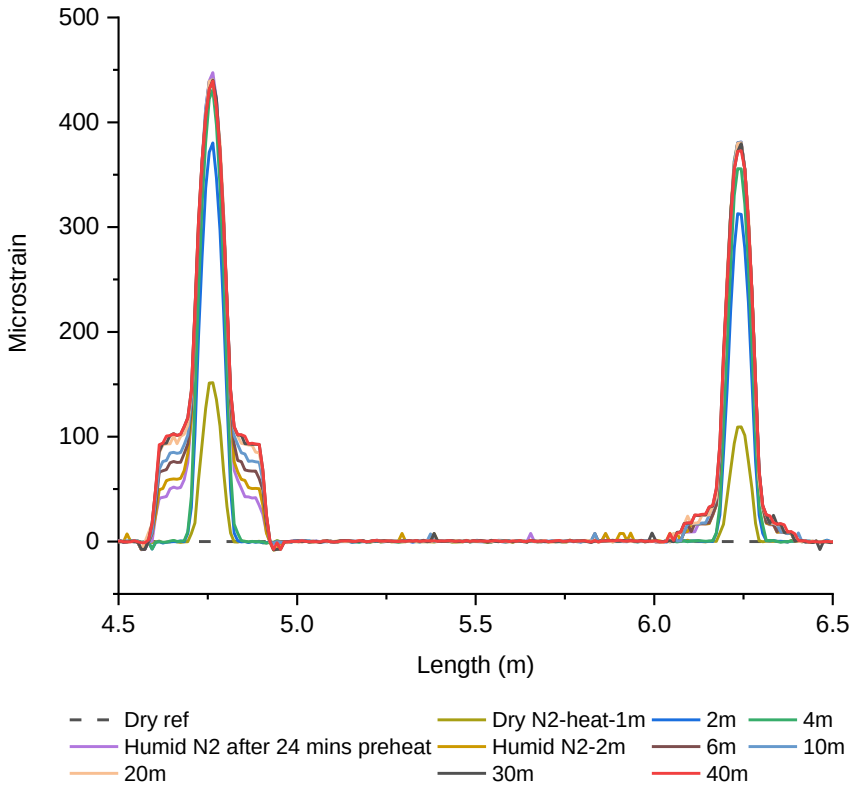

Figure 27. Effect of temperature during 75% RH humidity (glass tube preheated to 45 C).

The fiber in the glass tube was then preheated to 45 ^{o}C, which induced positive microstrain (over 400 microstrains on both regions) as shown in Figure 27. No new reference was set because the strain change on the fiber region without polymer jacket will be due to temperature, while the region with the polymer jacket will be due to both temperature and humidity. The difference between the two regions will indicate the strain due to humidity alone. When 75% RH was introduced to the glass tube with the fiber, positive microstrains was induced in the region of the fiber with the polymer jacket over time, as shown in Figure 27. This demonstrates that distributed humidity/water molecule monitoring can be sensed above RT.

7. OPTICAL FIBER-BASED CORROSION SENSOR WITH Fe/SiO_2 COATING

As reported earlier in this thesis and in previous studies, a distributed corrosion sensor using electrolessly coated Ni and Fe thin film on optical fiber has been demonstrated.[44] To improve sensing ability, a Fe/SiO_2 composite is coated on coreless optical fiber as sensing layer. The section of coreless fiber (cladding diameter of 125µm without a core) was spliced between two multimode fibers to construct a multimode-coreless-multimode (MCM) fiber structure. The multimode fiber has a cladding diameter of 125 µm containing a 50µm diameter core allowing light to travel in many modes simultaneously with minimum attenuation. When the light enters the coreless section, it interacts directly with the Fe/SiO_2 layer.

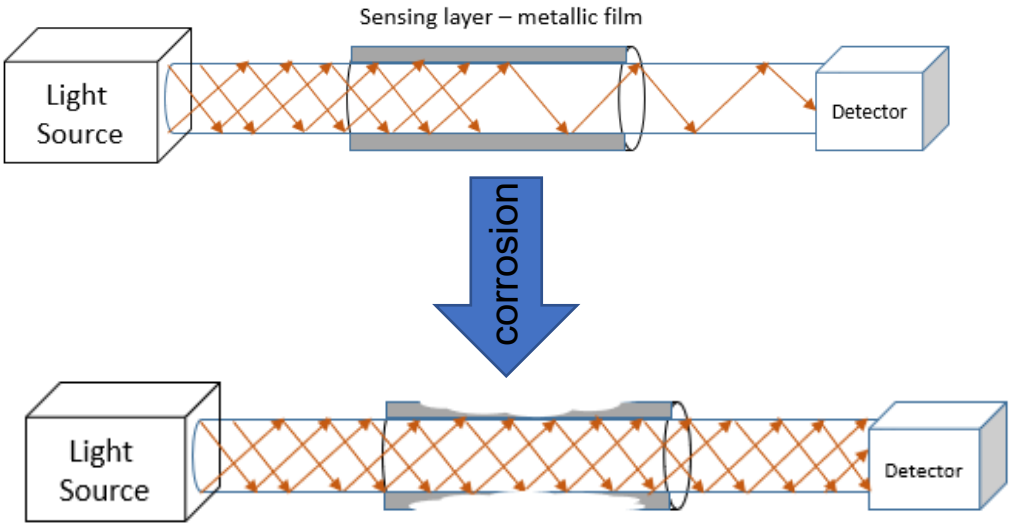

Figure 28. Schematic of light transmission through coreless fiber for corrosion sensor.

As shown in Figure 28, as light is transmitted through the coreless fiber with a metallic sensing layer, the light is absorbed by the metallic film and less light is

transmitted. As the metallic film corrodes/dissolves, the absorption decreases and more light is transmitted and detected by the detector (spectrometer).

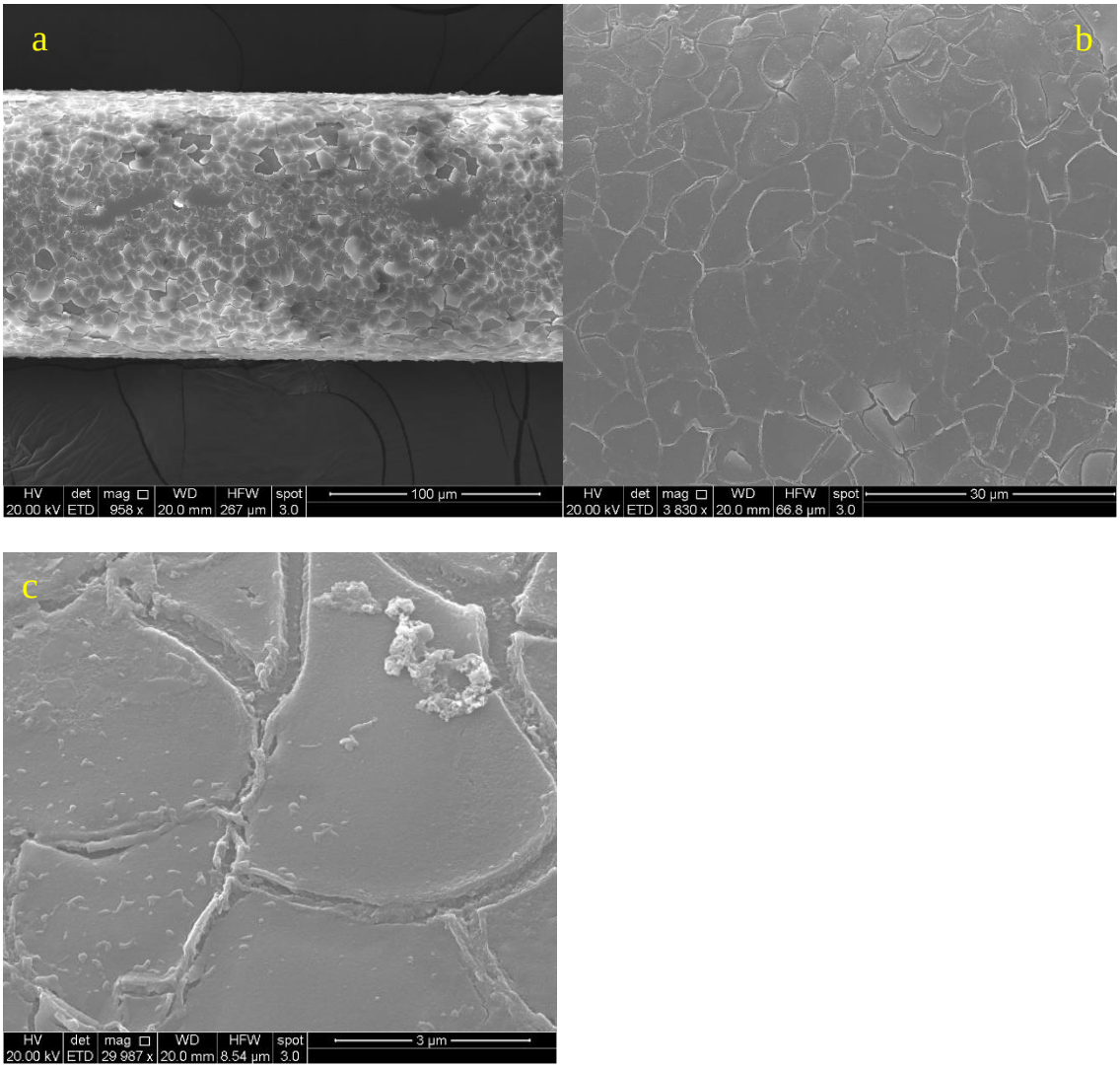

Figure 29. SEM of (a) the surface of SiO_2 made in basic TEOS sol-gel, (b) Fe film electrolessly coated on the SiO_2 and (c) dissolved in HCl solution of pH = 2.

First, to make the Fe/SiO_2 layer, the SiO_2 was synthesized by sol-gel method either in basic or acidic conditions and dip coated on the fiber. Then, during Fe thin film electroless deposition on the SiO_2 layer and dissolution of the Fe film, light transmission

measurements were taken. The light absorption by the Fe/SiO_2 composite gives an optical response which acts as the corrosion indicator.

The SiO_2 in basic condition was synthesized by mixing mole ratio 1:48:0.09:20 of TEOS:EtOH:NH_4OH:H_2O (All reagents are ACS grade), stirring for 3 hours, dip coating (25 travels) on the coreless fiber and calcinating at 160 ^oC for 2 hours. SEM image of the surface of the SiO_2 layer shows a thin film with cracks, as shown in Figure 29a. However, after electrolessly depositing Fe film on the SiO_2, SEM image of the surface of the Fe/SiO_2 film (Figure 29b) reveal that the cracks were still present. Light transmission measurements were taken while coating the Fe film on SiO_2 layer and compared to measurement with Fe coating on coreless fiber without the SiO_2 layer. The light source was a UV-Vis/IR source.

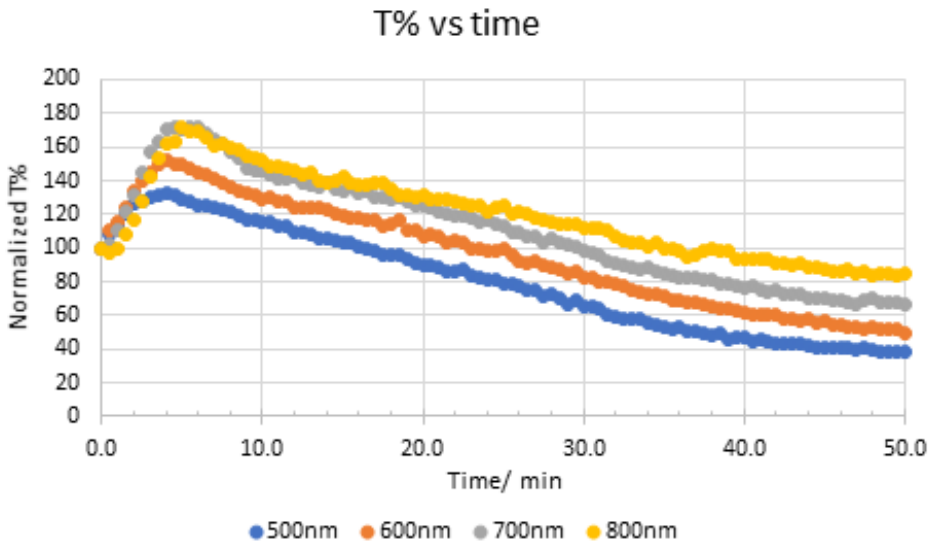

Figure 30. Transmittance during Fe plating on Coreless fiber without SiO_2

In Figure 30, the transmittance of light through the coreless fiber as Fe was deposited on the bare fiber is shown and will act as a control. At time zero, the electroless plating process starts, and the increase in transmission was due to the characteristic H_2

evolution during electroless Fe plating. As the H_2 bubbles with lower refractive index forms on the surface of the fiber, more light is transmitted along the fiber until the first Fe film replaces the bubbles on the surface of the fiber (within 5minutes as shown in Figure 30). As Fe film is deposited on the coreless fiber, less light is transmitted as shown by the decrease in transmittance at different wavelengths in Figure 30. The average change in normalized T% was 95% during electroless Fe plating on coreless fiber.

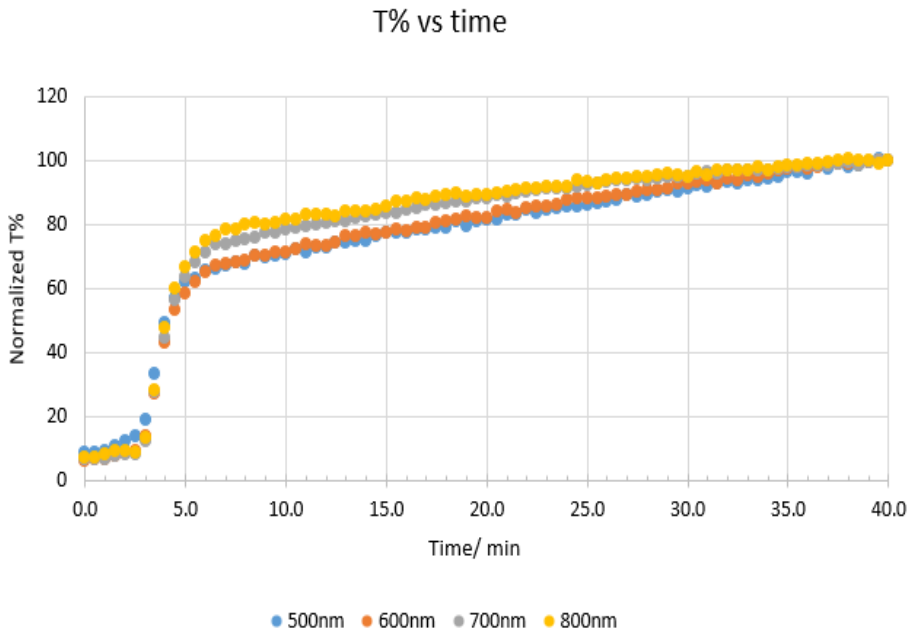

Figure 31. Transmittance during dissolution on Coreless fiber without SiO_2 (HCl solution, pH = 2)

The transmission measurement was also taken during the dissolution of the same Fe coated coreless fiber. In Figure 31, the Fe film dissolved within 5 minutes in HCl solution of pH 2. As the Fe film dissolved, the normalized transmittance increased until all the Fe film was dissolved, as shown in Figure 31.

The same experiment described above was carried on the coreless section of the MCM fiber with the Fe/SiO_2 composite. Before electroless plating, the coreless fiber with

the SiO_2 was pretreated with 10M NaOH, sensitized in $SnCl_2$ and activated in $PdCl_2$ with rinsing and drying in N_2 in between. The light transmission results during electroless Fe plating is shown in Figure 32.

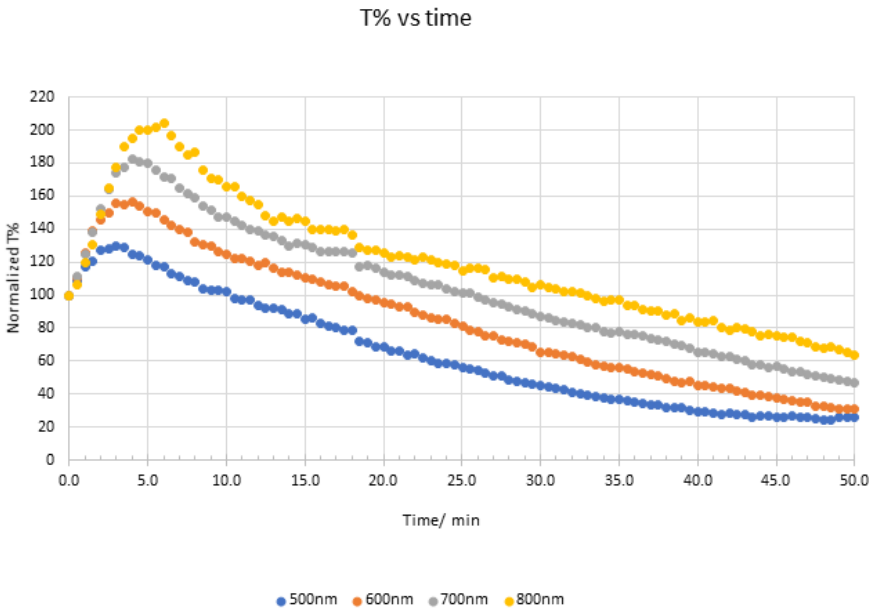

Figure 32. Transmittance during Fe plating on Coreless fiber with SiO_2 synthesized in alkaline conditions

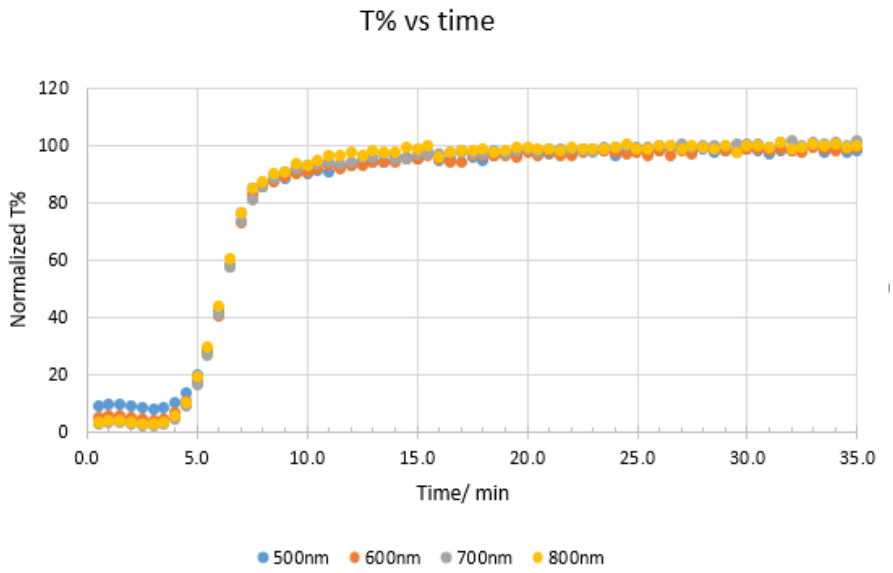

Figure 33. Transmittance during dissolution on Coreless fiber with SiO_2 synthesized in alkaline condition (HCl solution, pH = 2)

The average change in normalized T% was 127.5%, which is higher than the 95% without the SiO_2. This preliminary result demonstrates that Fe/SiO_2 composite provides more sensitive sensing ability. The transmission results during the dissolution of the Fe film on the Fe/SiO_2 composite layer in HCl solution of pH 2 is shown in Figure 33. Majority of the Fe film dissolved within 7 minutes.

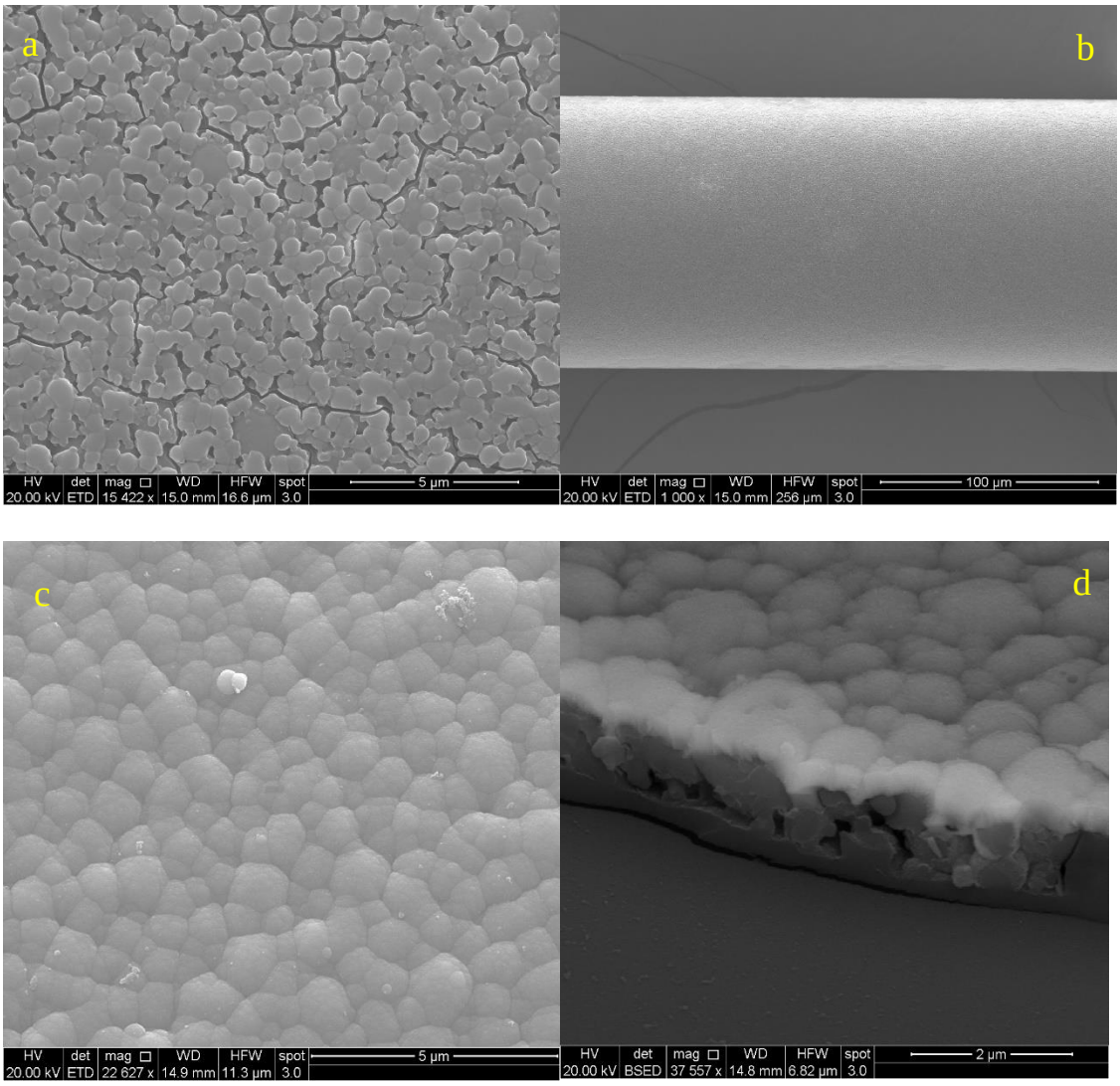

Figure 34. SEM of the surface of (a) SiO_2 coated coreless fiber, (b) lower magnification to show the uniformity of porous SiO_2, (c) electrolessly Fe coated film on SiO_2, and (d) backscattered electron image showing fiber, SiO_2, and top Fe film

Although there was an initial 34% increase in optical response when the Fe/SiO_2 is the sensing layer compared to just the Fe film, an improvement could be made in the SiO_2 coating for a more sensitive response. A more porous SiO_2 layer (Figure 34 (a)) was synthesized by mixing 10 mL TEOS, 5 mL EtOH, and 1.5 mL 0.1 M H_2SO_4, stirring for 3 hours before dip coating (5 travels) on the fiber and letting dry at RT. The SiO_2 layer is porous with a network that is uniformly coated, as shown in Figure 34 (a) and (b). The Fe film was electrolessly coated on the SiO_2 layer, which shows a close-packed morphology without cracks, as seen in Figure 34 (c). In Figure 34 (d), the backscattered electron image shows a brighter top layer (Fe film) and the middle layer (SiO_2) on the fiber surface.

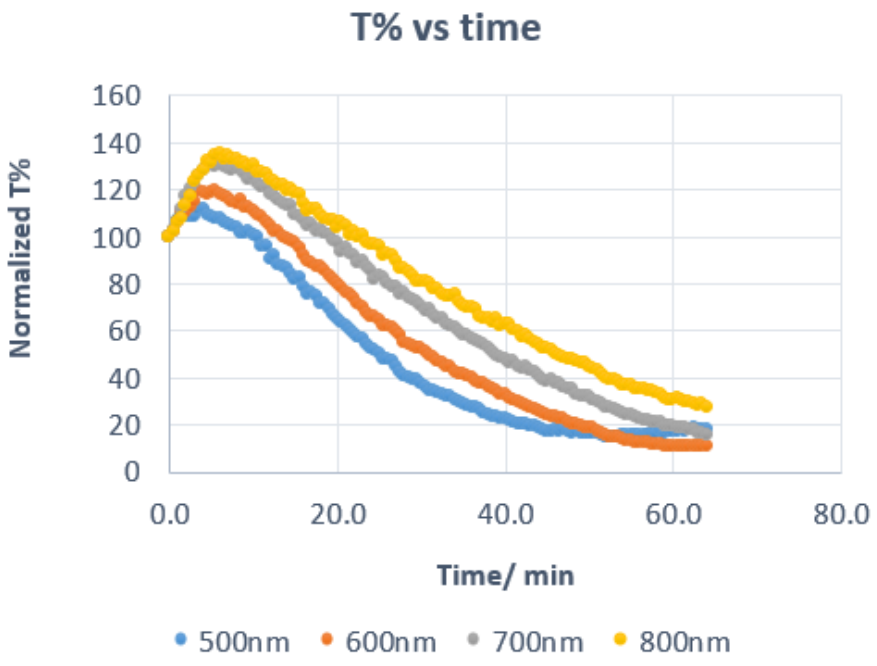

Figure 35 Transmittance during Fe plating on Coreless fiber with SiO_2 synthesized in acidic condition.

Transmission results during electroless Fe plating on the SiO_2 layer prepared in acidic conditions show the same trend observed during coating on coreless fiber or SiO_2

synthesized in basic conditions, as shown in Figure 35. During the dissolution of the Fe film on the Fe/SiO_2 composite in HCl solution of pH 2, the transmission results in Figure 36 show that Fe film dissolved within 10 minutes which is longer than the previous results reported in this study.

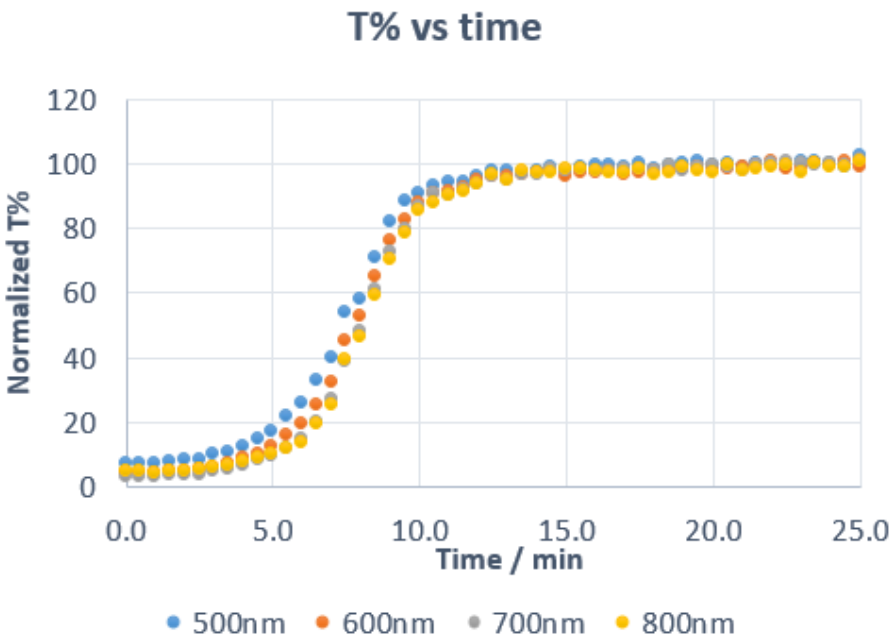

Figure 36. Transmittance during dissolution on Coreless fiber with SiO_2 synthesized in acidic condition (HCl solution, pH = 2)

In summary, preliminary results show that the Fe/SiO_2 composite, with the SiO_2 synthesized in basic sol-gel, improved the optical response. SiO_2 layer synthesized in an acidic sol-gel method produced a porous morphology and the dissolution took a longer time when compared to SiO_2 synthesized in basic conditions or on bare coreless fiber. This porosity or roughness increased the sensitivity of distributed corrosion sensor quality. A more detailed study is needed to confirm the finding and verify the hypothesis on increased sensitivity.

8. CONCLUSIONS ON ELECTROLESS PLATING FOR SENSORS

1. Nickel, copper, and iron films were successfully electrolessly coated on an optical fiber. SEM images show uniform coating when the pretreatment of the fiber includes rinsing and drying under N_2 after sensitization and activation.
2. A 5-meter long SM fiber was electrolessly coated on an SM optical fiber in 52 minutes to demonstrate the possibility of a distributed corrosion sensor at a longer distance.
3. An electrolessly coated optical fiber for distributed corrosion monitoring was demonstrated by showing electroless nickel deposition induced negative microstrain while dissolution in 1M HCl solution induced positive microstrain at the region of interest along the optical fiber. The contribution by electroless Ni plating only on the strain change was established by discriminating the contribution of temperature. In 50 mins, electroless Ni deposition induced 153 microstrains on the SM optical fiber.
4. When a commercial off-the-shelf SM optical fiber with dual-layer polymeric jacket was exposed to DI water, it induced positive microstrain (80 microstrains). This value is about one order of magnitude larger than has been reported on similar sensors. A linear relationship was established between strain change and different RH levels to which an SM fiber with dual-layer polymer jacket was exposed.
5. Initial results show that Fe/SiO_2 composite coated on the optical fiber increased corrosion sensing ability by 34%. A more porous SiO_2 layer was synthesized in

acidic conditions and is a promising intermediate layer to increase the sensing ability of optical fiber-based corrosion sensor.

9. ION INTERCALATION INTO VANADIUM SULFIDE COMPOUNDS

9.1 Introduction

Globally, battery manufacturing capacity will more than double by 2021 to about 280,000 megawatt-hours.[47] Rechargeable batteries make up a significant fraction of battery manufacturing. A rechargeable battery cell has two electrodes, the anode, and the cathode, which are separated by an electrolyte. In the case of solid electrodes, an electrolyte-permeable separator separates them. Electrochemical reactions at the anode and the cathode produce ions and electric charge. The ions are conducted by the electrolyte, and electrons are forced to pass through the outside of the cell. Current collectors at the anode and the cathode deliver electric current to and from the external circuit. During discharge, electrons and ions flow from the anode to the cathode. On charge, an applied electric field forces the electrons and ions to flow back from the cathode to the anode.[48] Lithium-ion technology has dominated the rechargeable battery industry because of its high energy density and portability.

High cost, safety issues, and charge storage capacity limit lithium-ion technology. These problems have sparked new interest in rechargeable batteries with multivalent ions like magnesium ion (Mg-ion). Magnesium is divalent, cheaper than lithium, easy to handle, and environmentally friendly. It has 1.85 times the theoretical volumetric capacity of lithium.[49] Passivation and choice of cathode materials have hindered Mg-ion technology. Passivation produces a surface thin film on the metal anode that prevents reversibility of magnesium ions. Electrolytes from magnesium organo-halo-aluminate complexes in ether solvents have significantly reduced passivation problems.[50] The choice of cathode material remains elusive. Theoretical predictions have shown high

magnesium ion mobility in six-coordination, spinel close-packed frameworks.[51] Mg-ions have been reported to favor octahedral environment in oxides and sulfides.[52] This project focuses on investigating vanadium sulfides compounds, $A_xV_5S_8$, $A_xV_6S_8$, and V_5S_8 as candidate cathode materials for Mg-ion batteries. A is an alkali metal, or monovalent cation and x = 0 – 0.8.

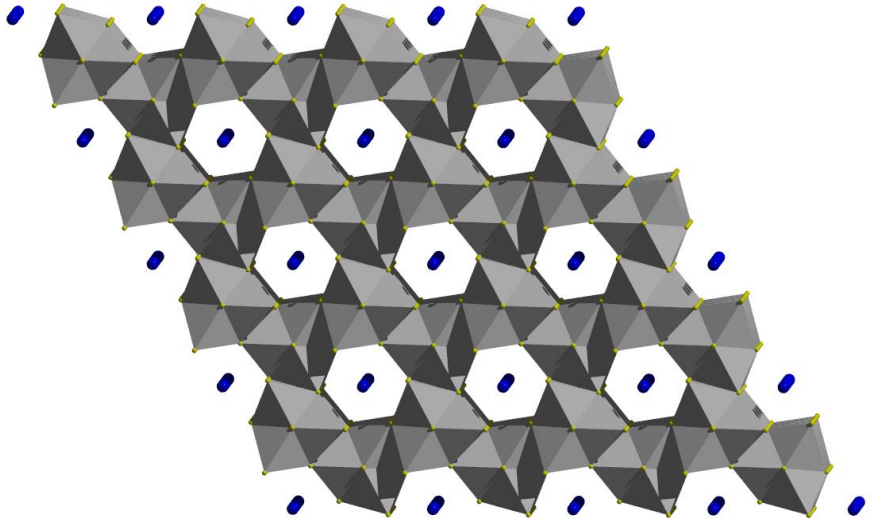

Figure 37. Schematic of the structure of $A_xV_6S_8$. The "purple" ions are the intercalated ion the large hexagonal channel.

$A_xV_6S_8$ has a hexagonal unit cell formed from a distorted VS_6 octahedral sharing faces and edges, with large hexagonal channels capable of intercalating ions (Figure 37).[53] $A_xV_5S_8$ has a monoclinic structure (Figure 38) with slightly distorted VS_6 octahedra sharing edges and faces, and parallelogram-shaped tunnels available for ion insertion.[54] Both $A_xV_5S_8$ and $A_xV_6S_8$ have short V-V zigzag chains that make both metallically conductive.[51,52] V_5S_8 has a monoclinic structure related to the NiAs structure, with metal vacancies in 3/8 of the available sites.[55]

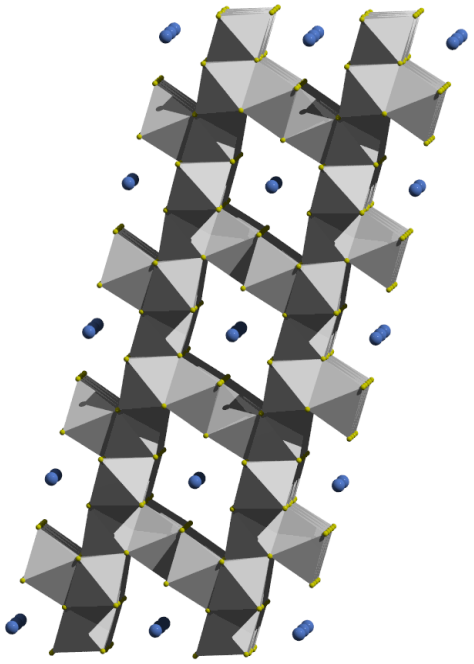

Figure 38. Schematic of the structure of $A_xV_5S_8$; the "blue" ions are the intercalated anion.

In this work, $K_xV_6S_8$, $K_xV_5S_8$, $Rb_xV_6S_8$, $Rb_xV_5S_8$, and V_5S_8 were synthesized and characterized using powder XRD. Electrochemical properties of the $K_xV_5S_8$, $Rb_xV_6S_8$, and V_5S_8 were studied by cyclic voltammetry and chronopotentiometry.

9.2 Experimental

Stoichiometric mixtures of vanadium sulfide compounds were synthesized in evacuated sealed quartz tubes. All chemicals were American Chemical Society (ACS) reagent grade. The stoichiometry used to synthesize the products is described by Equations 29 – 33, with a total mass of 200 mg.

$$1/2\ K_2S_2 + 5V + 7/8S_8 \rightarrow K_xV_5S_8 \quad (29)$$

$$1/2\ K_2S_2 + 6V + 7/8S_8 \rightarrow K_xV_6S_8 \quad (30)$$

$$1/2\ Rb_2S_2 + 5V + 7/8S_8 \rightarrow Rb_xV_5S_8 \quad (31)$$

$$1/2\ Rb_2S_2 + 6V + 7/8S_8 \rightarrow Rb_xV_6S_8 \quad (32)$$

$$5V + S_8 \rightarrow V_5S_8 \quad (33)$$

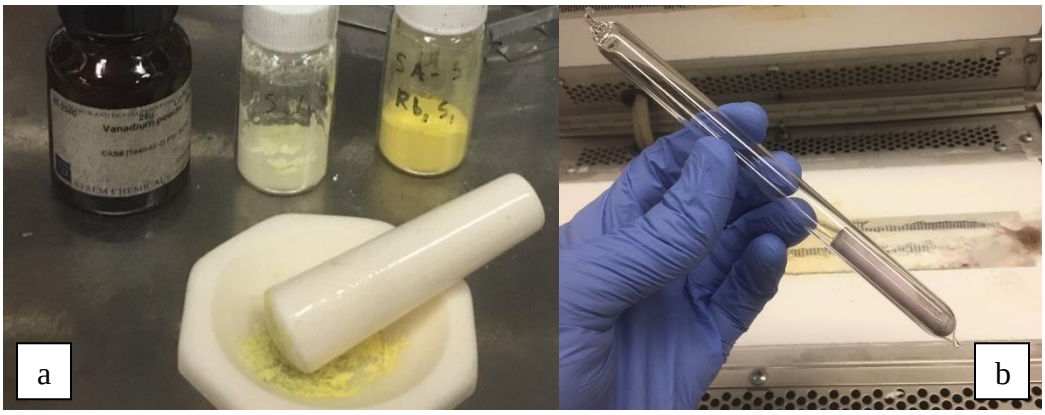

Figure 39. (a) Stoichiometric chemical mixture ground in the mortar and pestle (b) Crucible containing stoichiometric mixture to be annealed, sealed in a quartz tube

All procedures were done in a glove box; the mixtures were ground together in a mortar and pestle before transferring to an alumina crucible (Figure 39). The crucible was sealed in a quartz tube and annealed at 750 ^{o}C for 24 hours before slowly cooling.

The products were handled and analyzed under argon. Samples of $A_xV_6S_8$, $A_xV_5S_8$, and V_5S_8 were characterized using Cu K_α radiation powder Bruker D8 Powder X-ray Diffractometer (Figure 40).

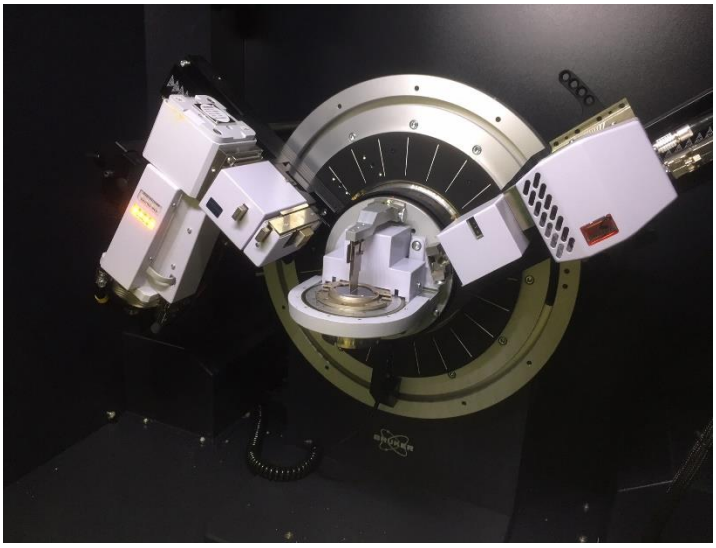

Figure 40. Bruker Powder X-ray Diffractometer, showing the sample holder stage, the x-ray source, and the detector.

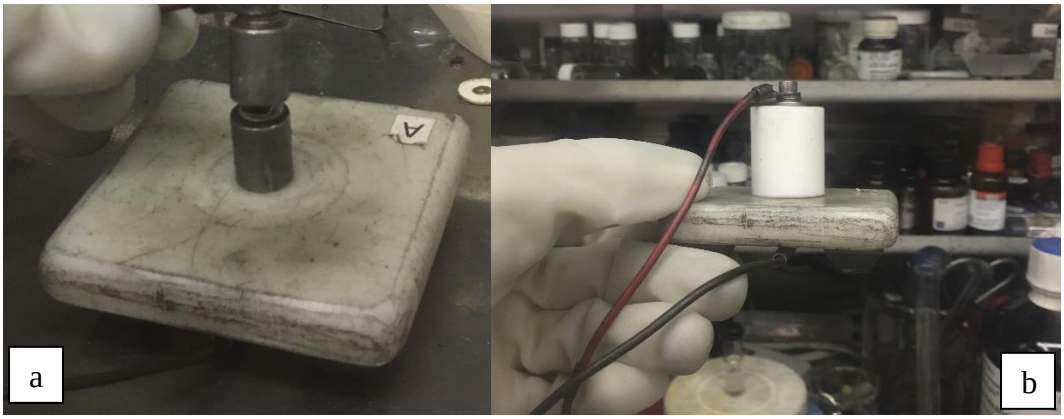

Figure 41. Picture of the electrochemical cell (a) the Li metal anode, 80% VS cathode, Li-ion electrolyte, glass frit, Kynar and graphite between current collectors (b) the completed cell in a white Teflon case

Electrochemistry cell assembly consists of steel electrodes, lithium metal, 1 M $LiClO_4$ in 1:1 ethylene carbonate (EC) and diethyl carbonate (DEC) electrolyte, glass frit spacer, and the active material (Figure 41). The active material was prepared by mixing 80% vanadium sulfide compound cathode with 10% Kynar and 10% graphite by mass at a scale of approximately 50 mg. A few drops of dimethylformamide was added, and this mixture was spread onto a stainless-steel electrode. The mixture was dried onto the electrode on a hot plate, and the process was repeated until 15-20 mg of material was deposited on the electrode. The electrodes were assembled within a Teflon sleeve and attached to the potentiostat using electrical feed-throughs in the glove box.

9.3 Results/Discussion

The X-ray diffraction pattern of each vanadium sulfide compound should be distinct for each different phase, specific chemistry, and atomic arrangement. To investigate the structure of as-prepared $K_xV_5S_8$, the XRD peaks were matched to a known $K_xV_5S_8$ pattern in the International Center for Diffraction Data database (ICDD), represented as a red stick pattern in Figure 42. The XRD pattern of $K_xV_5S_8$ shows two main sharp and strong diffraction peaks ($2\theta = 10.9^o$ and 21.8^o), and several peaks in the range $33\text{-}50^o$ 2θ. The intensities of the low angle reflections are a poor fit to the reference, perhaps due to preferred orientation effects, but the high angle reflections show that $K_xV_5S_8$ was successfully synthesized by this method.

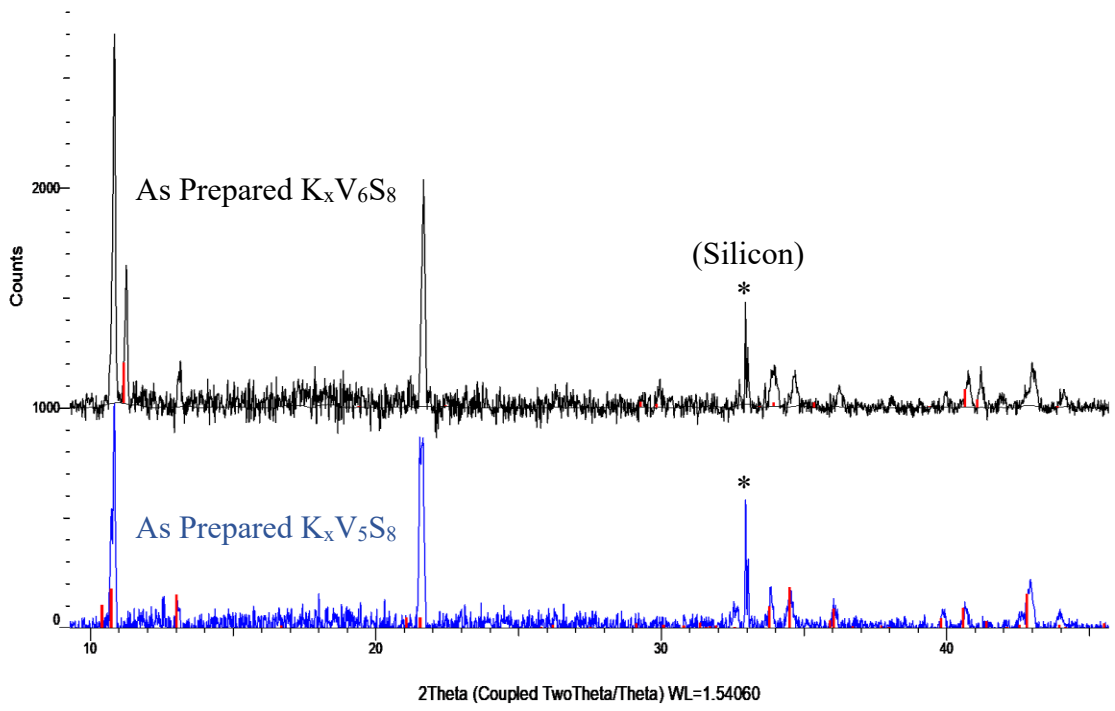

Figure 42. XRD pattern of $K_xV_5S_8$ and $K_xV_6S_8$ showing peak impurity in the $K_xV_6S_8$ pattern. The red box shows $K_xV_5S_8$ peaks present in the $K_xV_6S_8$ pattern

For $K_xV_6S_8$ phase, the as-prepared XRD pattern (Figure 42, black pattern) was matched with a known $K_xV_6S_8$ phase pattern in the ICDD database. Although three main sharp and strong peaks ($2\theta = 10.9^o$, 11.1^o and 21.8^o) are present, the red sticks from the $K_xV_6S_8$ reference pattern show that only the peak at $2\theta = 11.1^o$ is from the $K_xV_6S_8$ phase. The peaks at $2\theta = 10.9^o$ and 21.8^o are identical to those observed in $K_xV_5S_8$, indicating phase impurity. Although potassium is an effective alkali metal to synthesize the $A_xV_5S_8$ framework, it is not sufficient for $A_xV_6S_8$ framework.[56] A larger metal, rubidium, was then used to replace potassium.

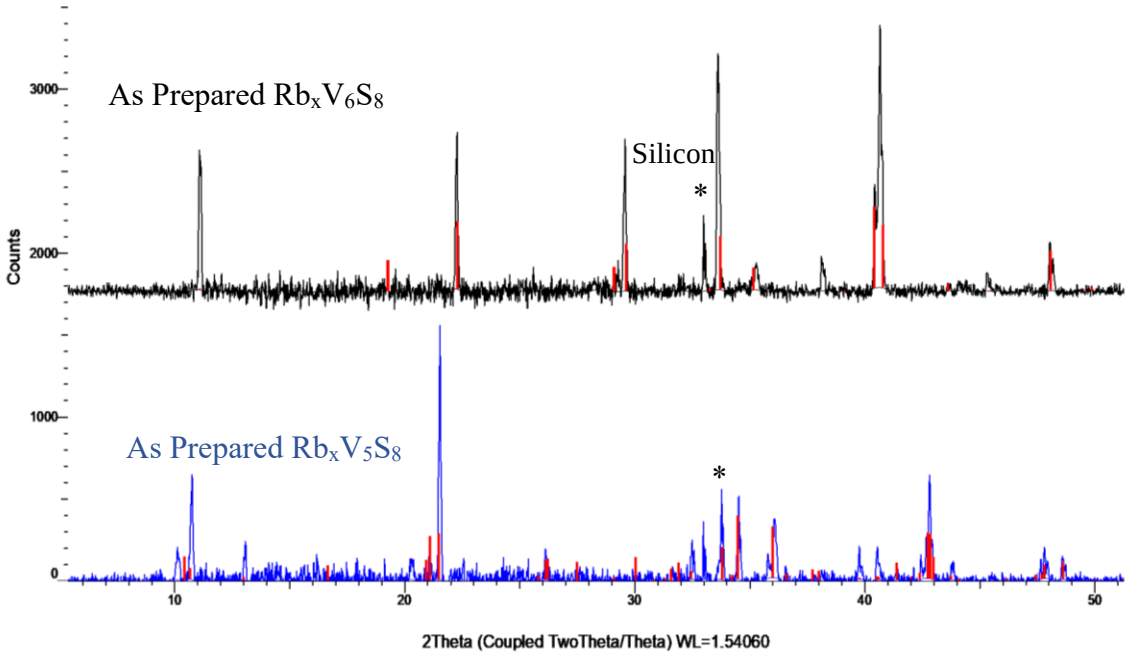

Figure 43. XRD pattern of $Rb_xV_5S_8$ and $Rb_xV_6S_8$ fit with $Tl_xV_5S_8$ and $Tl_xV_6S_8$

The XRD pattern results of as-prepared $Rb_xV_5S_8$ and $Rb_xV_6S_8$ were matched to known patterns of each phase in the ICCD database, as shown in Figure 43. The red sticks in Figure 43 are the peaks from the reference pattern. The $Rb_xV_5S_8$ show main strong diffraction peaks are $2\theta = 21.5^o$, 34.5^o, 36^o, and 43^o while for $Rb_xV_6S_8$, $2\theta = 29.5^o$,

33.5°, 41.5° and 48°. Since the peaks from the two distinct phases do not overlap, using rubidium is an effective alkaline metal to synthesize the $A_xV_5S_8$ and $A_xV_6S_8$ frameworks.

Cyclic voltammetry (CV) scan of $K_xV_5S_8$ cathode against lithium metal anode with Li-ion electrolyte was performed to analyze the use of $A_xV_5S_8$ as a potential cathode material. A CV is used to study the reduction and oxidation processes of a given electrochemical reaction.[57] The measurements here have a voltage range of 0.5 – 3.5 V and a sweep rate of 0.5 mV/s for 3 cycles. In Figure 44, a very small oxidation peak is visible in the first scan (blue) at about 2.9 V, and no other significant reduction or oxidation peaks are observed (the solvent is responsible for the reduction current below 1 V). The integrated charge for the oxidation step was 18.85 mC. Although the oxidation peak indicates potassium may have been deintercalated, there was little indication of intercalation of Li^+. The breakdown of the $A_xV_5S_8$ framework during deintercalation is a possible reason for the lack of reduction or overall reversibility.

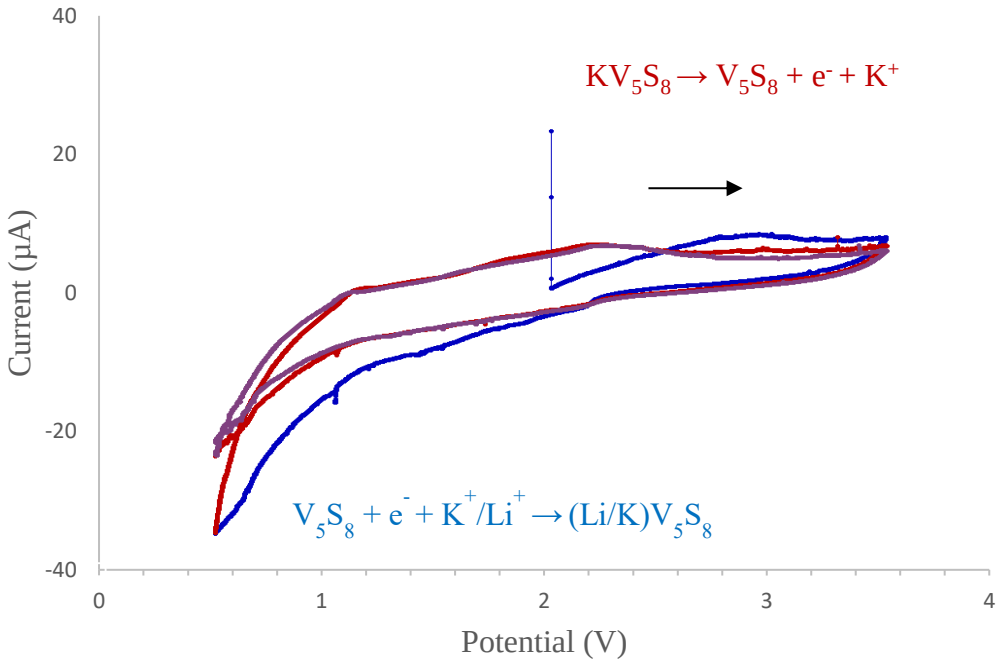

Figure 44. Cyclic voltammetry scan of Li-ion intercalation into $K_xV_5S_8$

In cyclic voltammetry, a known range of potential is applied, and the resulting current passed is recorded indicating the redox mechanism of the reaction. In contrast, chronopotentiometry investigates the potential required for the system to provide a given current. Applying constant current to the working electrode will cause an electroactive species' potential to change to a value enough to supply the applied current. Ideally, an intercalated species will maintain a steady potential during oxidation as an ion is deintercalated, resulting in a 'plateau' representing a stable solid solution range. Eventually, the electroactive species will no longer be able to sustain the applied current and the potential changes rapidly.[58] This phenomenon is indicated by the dotted red line in Figure 45.

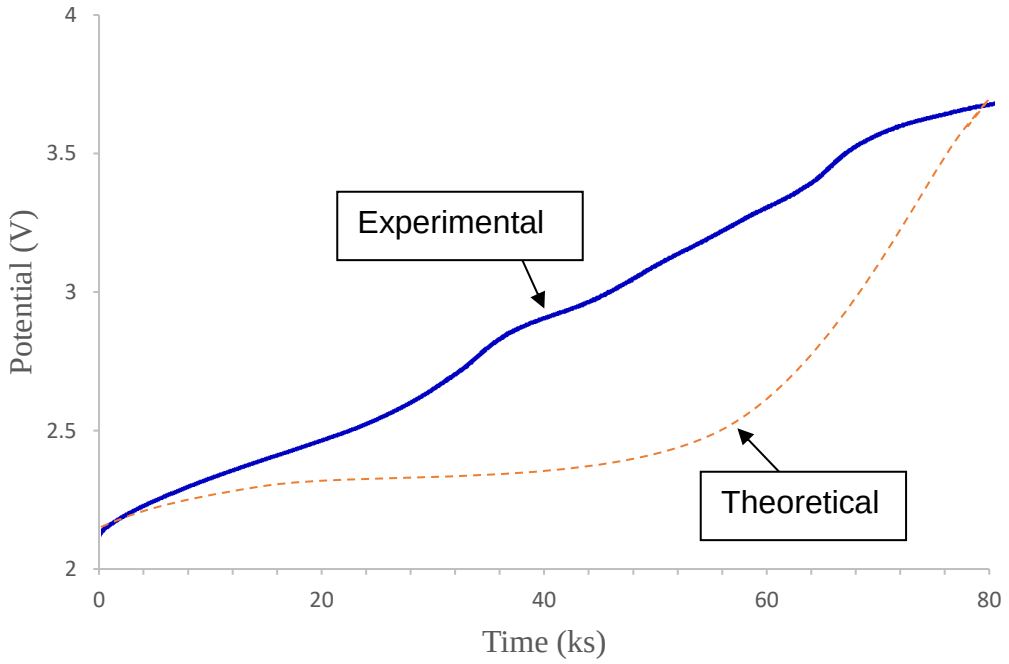

Figure 45. Chronopotentiogram obtained on $K_xV_5S_8$ cathode with $LiClO_4$ in 1:1 EC/DEC electrolyte by applying 16.2 µA current.

The theoretical capacity according to cyclic voltammetry (Table 8) is $K_{0.01}V_5S_8$. As shown in Figure 45, as 16.2 µA is applied, the intercalated potassium should have

maintained a steady potential during oxidation, indicated by the dotted red line in Figure 45. But, this was not the case, as shown by the rapid increase in potential.

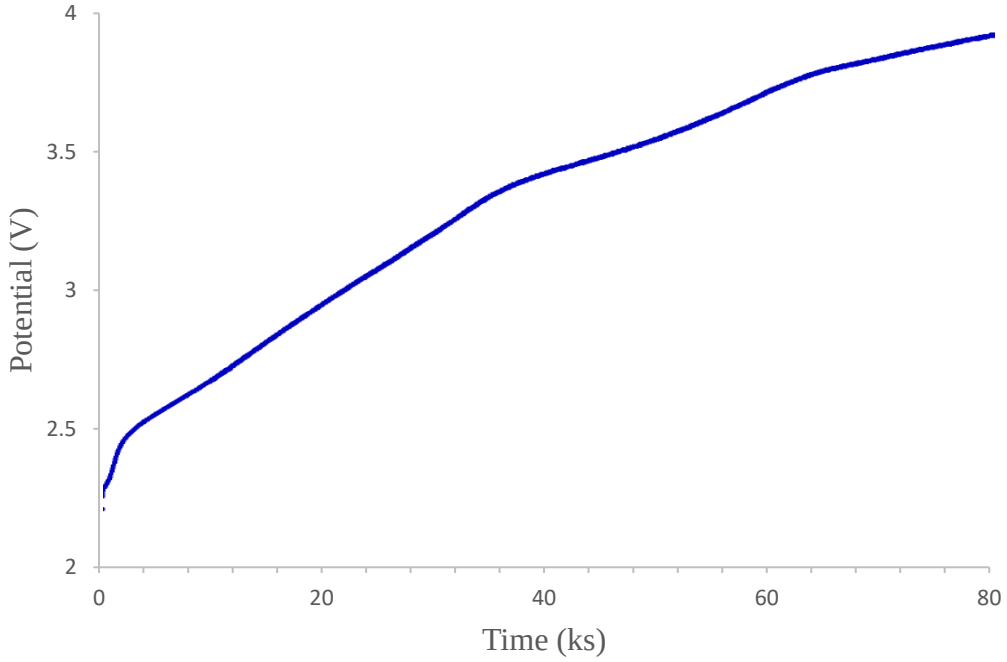

Figure 46. Chronopotentiogram obtained on $Rb_xV_5S_8$ cathode with $LiClO_4$ in 1:1 EC/DEC electrolyte by applying 21.5 µA current.

To determine the applied current for chronopotentiometry scan of $K_xV_5S_8$, the moles of $K_xV_5S_8$ (1.45×10^{-5} moles) in the working electrode was multiplied by 96 485 C (the charge in 1 mole of electron) and the product, 1.86 C was then divided by 86 400 s (24 hours) to give 16.2 µA. Then chronopotentiogram of $K_xV_5S_8$ in Li-ion electrolyte obtained by applying 16.2 µA of current shown in Figure 45 does not show any reduction potential plateau, matching the CV results. This shows that $K_xV_5S_8$ in this experiment is not electrochemically active. The chronopotentiogram of $Rb_xV_5S_8$ was also obtained with the same conditions as the $K_xV_5S_8$, as shown in Figure 46. The applied current for the chronopotentiometry of $Rb_xV_5S_8$ was calculated to be 21.5 µA from 1.93×10^{-5} moles of $Rb_xV_5S_8$ in 15.5 mg of active material. The chronopotentiogram follows the same trend

and confirms that there is not enough evidence to show that the $A_xV_5S_8$ framework is electrochemically active during this test.

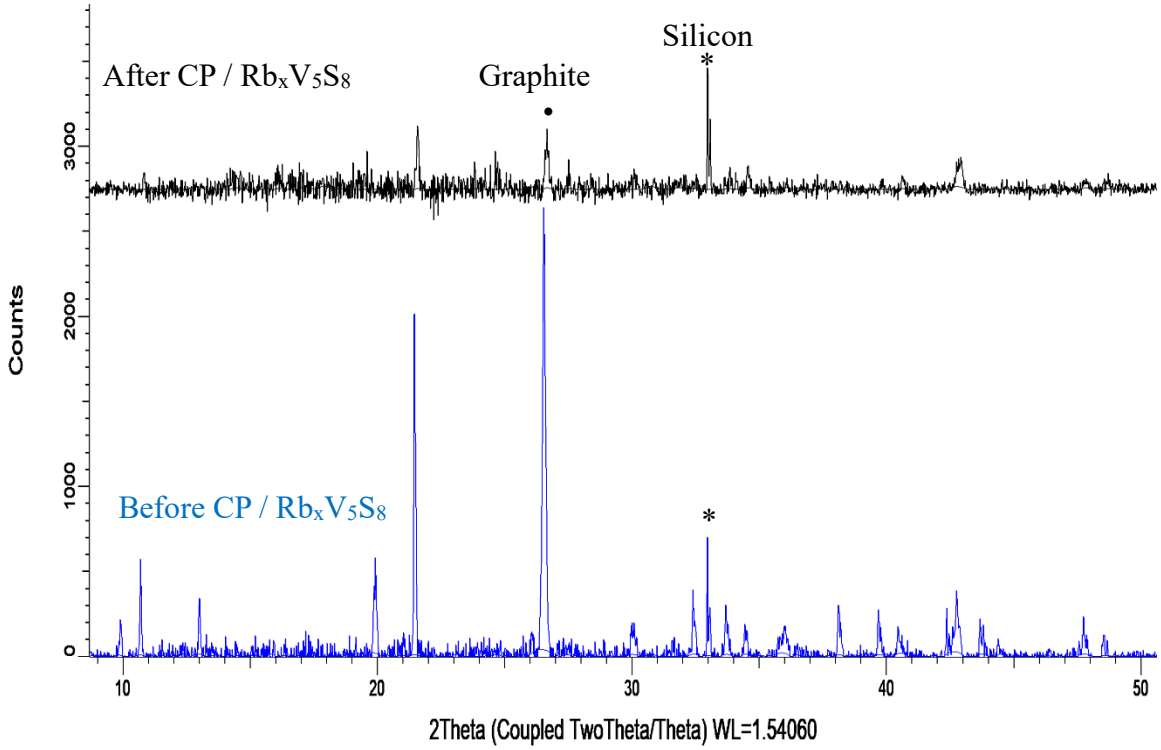

Figure 47. XRD pattern of before and after chronopotentiometry scans of $Rb_xV_5S_8$

The XRD pattern of the 80 % $Rb_xV_5S_8$ in the active cathode material was obtained before and after the chronopotentiometry measurement for comparison, as shown in Figure 47. After chronopotentiometry, the $Rb_xV_5S_8$ phase peaks between $2\theta = 30^o$ - 42^o, and 10^o – 20^o were no longer present. The peak at $2\theta = 21.5^o$ was diminutively short and weak. This confirms that during chronopotentiometry, the $A_xV_5S_8$ framework did not maintain its phase structure and is not electrochemically active.

The electrochemical activity of another vanadium sulfide compound, V_5S_8 was investigated. It should be emphasized that even though the formula of V_5S_8 resembled the alkali-metal intercalated structures described previously, it lacks channels. To characterize the V_5S_8, the X-ray diffraction pattern of as-prepared V_5S_8 was matched

against a known V_5S_8 peak pattern from the ICCD database (PDF 01-076-0719 V_5S_8 Vanadium Sulfide). The red sticks indicating the reference V_5S_8 pattern peaks matched with the as-prepared V_5S_8 peaks, as shown in the blue pattern in Figure 50. This confirms that the as-prepared V_5S_8 phase was phase pure. After 3 cycles of cyclic voltammetry with V_5S_8 cathode against a Li-anode and Li-ion electrolyte, XRD patterns were obtained, and as shown in the black pattern in Figure 48, the V_5S_8 diffraction peaks were still present, indicating that this structure is stable to the redox conditions applied.

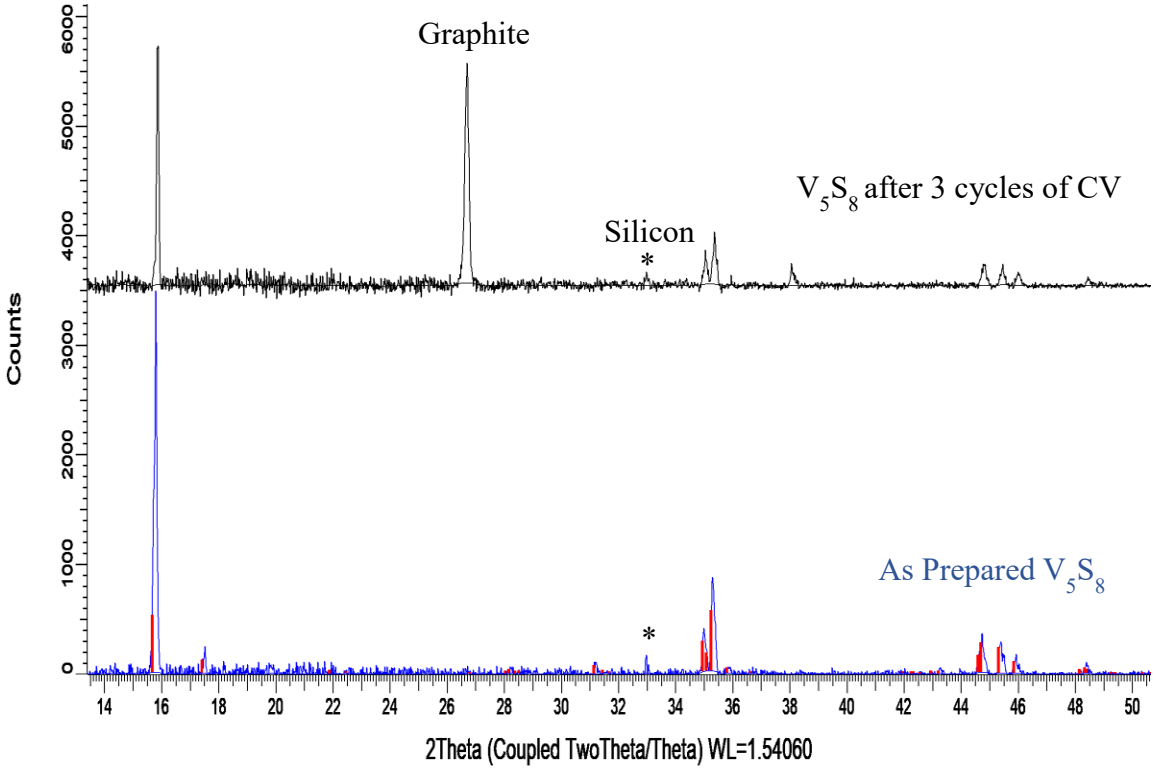

Figure 48. XRD pattern of as-prepared V_5S_8 before (bottom) and after (top) 3 cycles of cyclic voltammetry scan.

The reaction of V_5S_8 as a cathode was analyzed by the CV, as shown in Figure 49. The CV has a voltage range of 0.5 – 3.5 V and a scan rate of 0.5 mV/s. Since this material was not initially intercalated with an alkali metal, the first sweep was negative, in order to reductively intercalate lithium into the structure. The first reduction peak

appeared at 1.8 V (integrated charge of -137.4 mC) while the second and third reduction peaks appeared at 2.0 V (-67.95 mC).

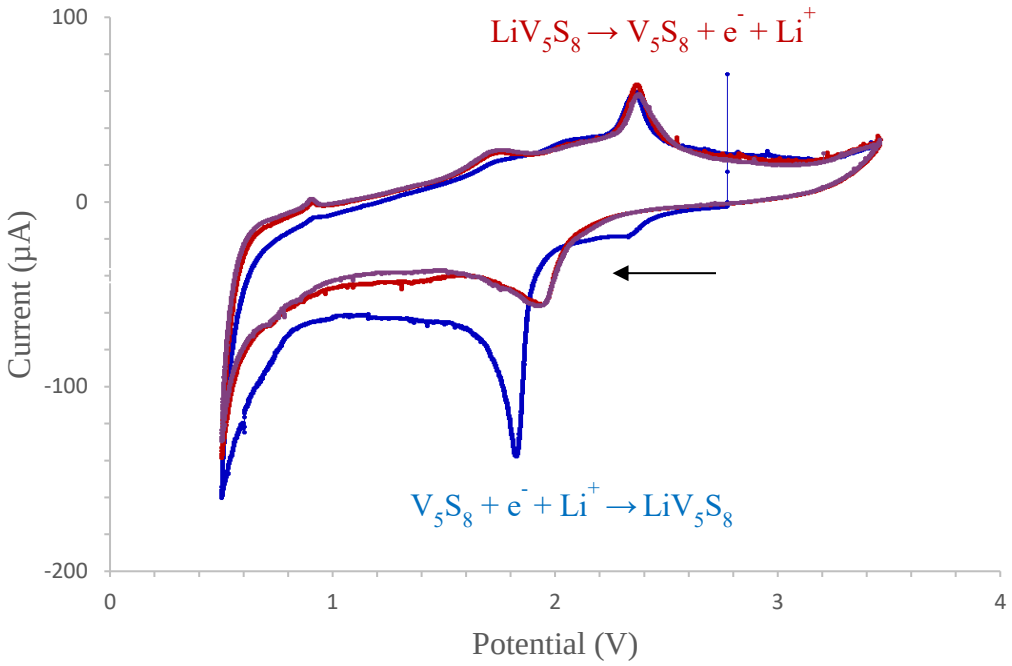

Figure 49. Cyclic voltammetry scan of Li-ion intercalation into V_5S_8

All three oxidation peaks appeared at 2.4 V (the integrated charge for the first scan was 42.27 mC and 53.66 mC for the subsequent scans). When compared to the theoretical capacity of 2.21 C, the V_5S_8 held only about 2% of the Lithium-ion, as shown in Table 8. The formation of $Li_xV_5S_8$ and V_5S_8 are consistent with the charge and discharge of the cell. This demonstrates that V_5S_8 is electrochemically active and shows significant oxidation and reduction peaks during cyclic voltammetry with a lithium anode.

Table 8 shows the chemical formula of the $Li_xV_5S_8$ and $K_xV_5S_8$ compounds after cyclic voltammetry. During oxidation of $K_xV_5S_8$, only about 1 % of potassium-ion was possibly oxidized. For the V_5S_8 compound, during the first reduction event, 6 % of Li-ion

was intercalated, but about half of that was deintercalated, indicating that V_5S_8 held on to small quantities of the Li-ion. Subsequently, during the reduction event of the second cycle, only about 3 % of Li-ion was intercalated and about 2 % deintercalated during oxidation event.

Table 8. Results from cyclic voltammetry of $K_xV_5S_8$ and V_5S_8 showing the redox mechanism.

Compound	**Oxidation / Reduction**	**Integrated capacity**	**Theoretical capacity**	**Chemical formula**
$K_xV_5S_8$	Oxidation	18.85 mC	1.40 C	$K_{0.01}V_5S_8$
V_5S_8	Reduction peak 1	137.4 mC	2.21 C	$Li_{0.06}V_5S_8$
	Oxidation peak 1	42.27 mC	2.21 C	$Li_{0.02}V_5S_8$
	Reduction peak 2	67.95 mC	2.21 C	$Li_{0.03}V_5S_8$
	Oxidation peak 2	53.66 mC	2.21 C	$Li_{0.02}V_5S_8$

9.4 Conclusion

1. $K_xV_5S_8$, $Rb_xV_5S_8$, $Rb_xV_6S_8$, and V_5S_8 were successfully synthesized, and their XRD pattern confirmed that each pattern contained a pure phase when matched with known reference patterns in the ICCD database. The XRD pattern for $K_xV_6S_8$ had $K_xV_5S_8$ peaks indicating phase impurity due to the small size of potassium.

2. Cyclic voltammetry of $K_xV_5S_8$ showed a small oxidation peak but no reduction peak, indicating the lack of reversibility or intercalation of ion. Chronopotentiometry data confirms that $K_xV_5S_8$ is not electrochemically active. Chronopotentiometry scan of $Rb_xV_5S_8$ shows that it is not electrochemically active, confirming that $A_xV_5S_8$ was not electrochemical active during this study.

3. XRD pattern of before and after 3 cycles of cyclic voltammetry of V_5S_8 show the oxidation and reduction peaks. This is surprising since this compound lacks the channel structure hypothesized to increase stability. Chronopotentiometry measurements are needed to measure the reversible capacity of this compound.

4. V_5S_8 was found to reversibly intercalate lithium and is a promising electrode material for further study.

5. Additionally, $Rb_xV_6S_8$ will be investigated for electrochemical activity. After confirming which structures are capable of reversible intercalation, magnesium ion intercalation studied will be conducted.

APPENDIX

OPTICAL MICROSCOPE IMAGE OF ELECTROLESS NICKEL PLATING IN A BASIC BATH

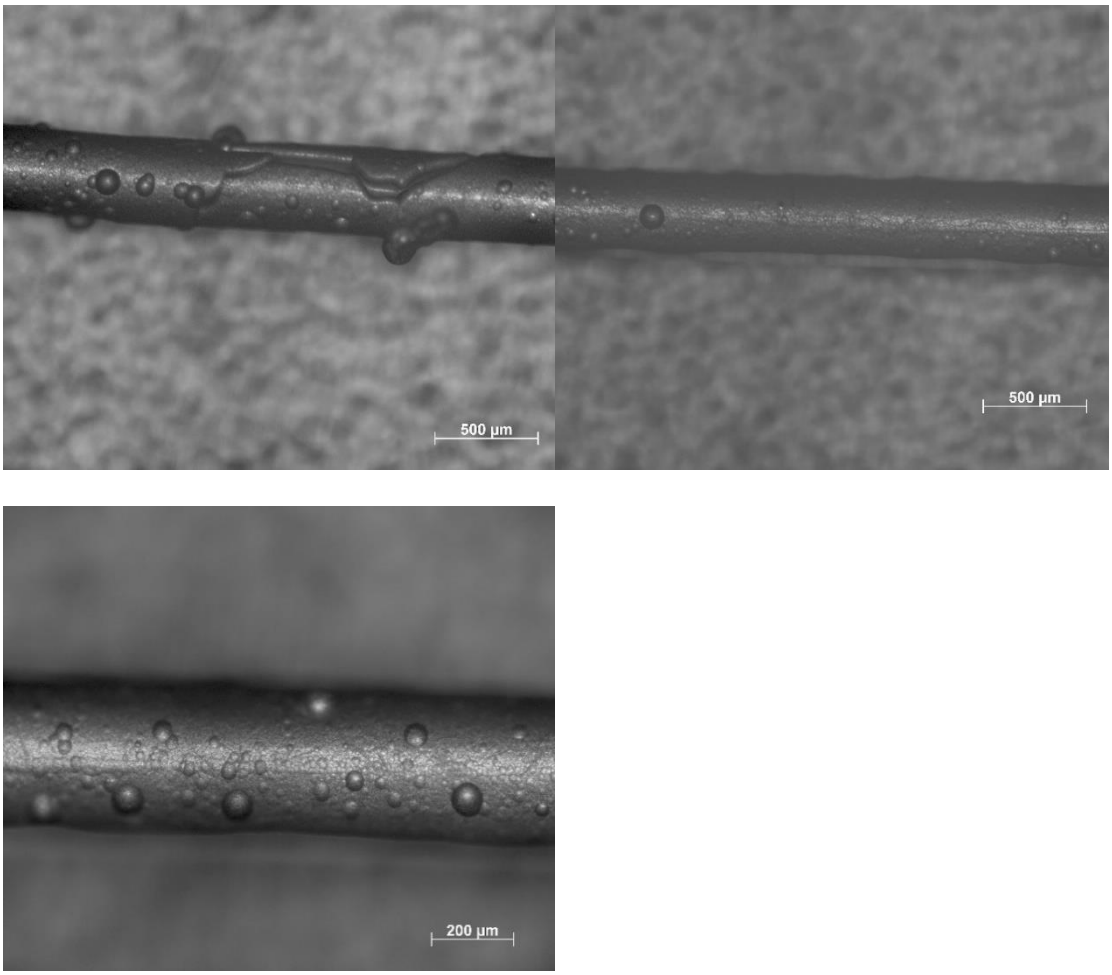

Figure A 1. Electroless nickel plating from plating bath composition in Table A1.

Electroless Ni Plating	Conc. (g/L)
$NiSO_4.6H_2O$	20.9
$Na_3C_6H_5O_7.2H_2O$	8.1
NH_4Cl	6.4
$NaH_2PO_2.H_2O$	14.8
pH	9
Plating time	1.5 hrs at 90 ^oC
	72 hrs at 34 ^oC

Table A 1. ENP bath composition

SEM IMAGES OF ELECTROLESSLY COATED FE AND NI ON SM FIBER

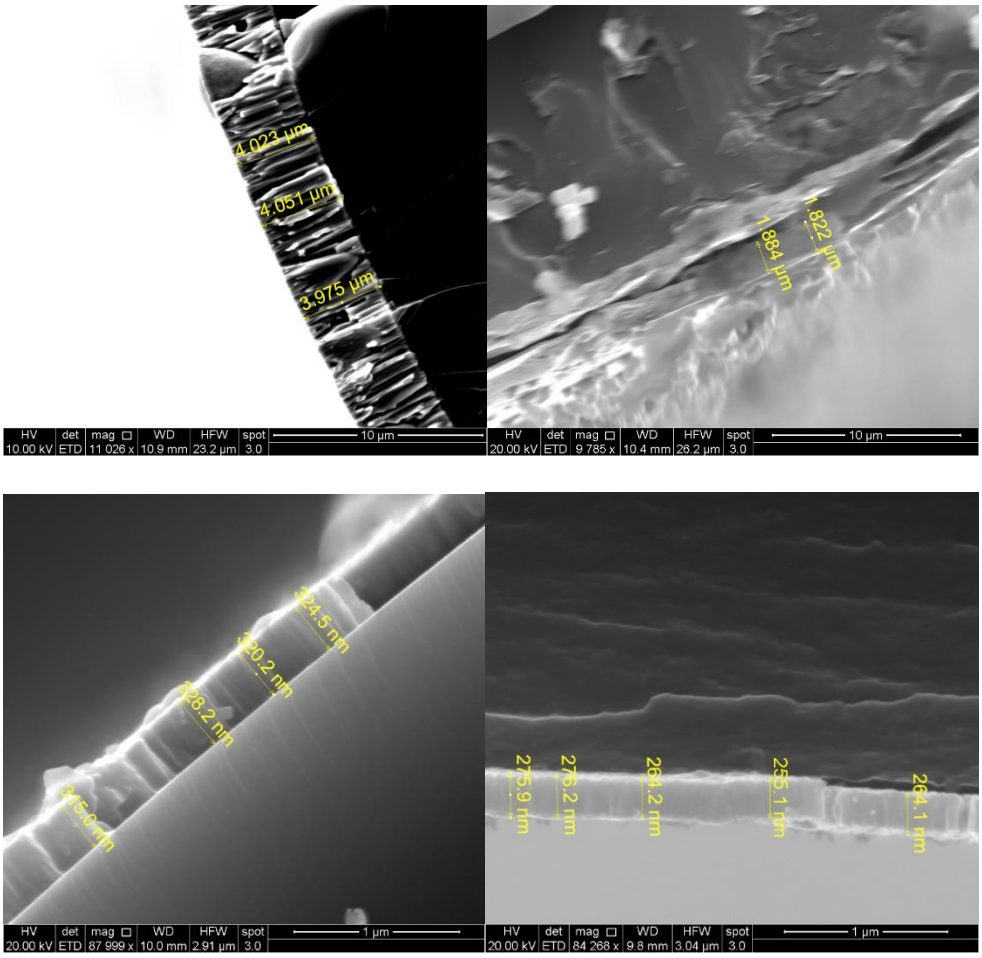

Figure A 2. SEM images of the cross-section of electrolessly coated (a) Ni film in fiber with polymer (b) Ni film on fiber without jacket (c) Fe film on fiber without polymer jacket (d) Fe film on fiber with a polymer jacket

ELECTROLESS PLATING BATH

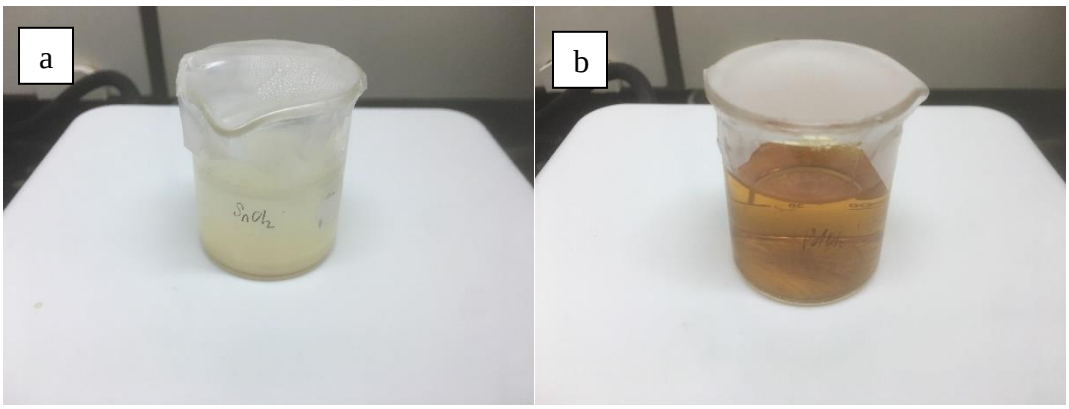

Figure A 3. (a) SnCl2 sensitization solution (b) PdCl2 activation solution

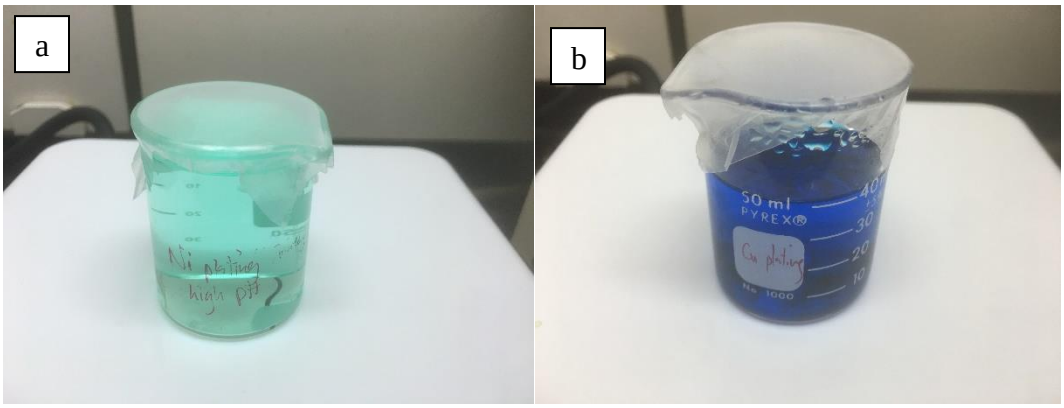

Figure A 4. (a) Electroless nickel plating bath (b) electroless copper plating bath

Figure A 5. Electroless iron plating bath

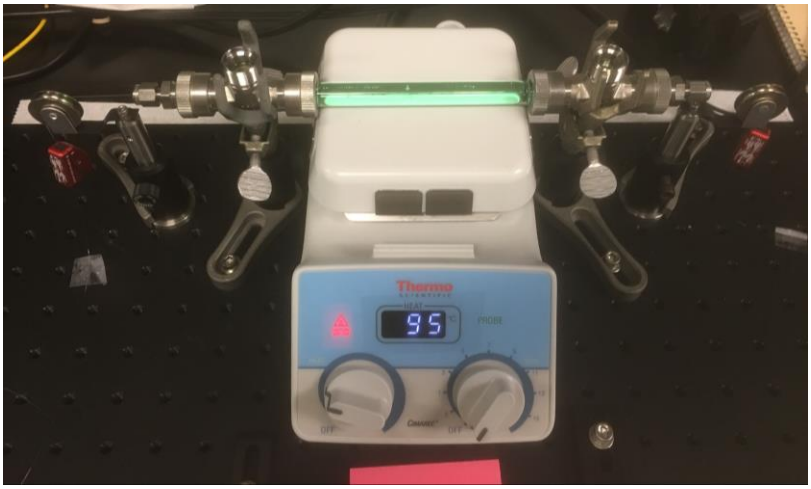

Figure A 6. Picture of electroless nickel plating set-up

MICROSTRAIN MEASUREMENTS SHOWING REVERSIBILITY AT DIFFERENT RH LEVELS

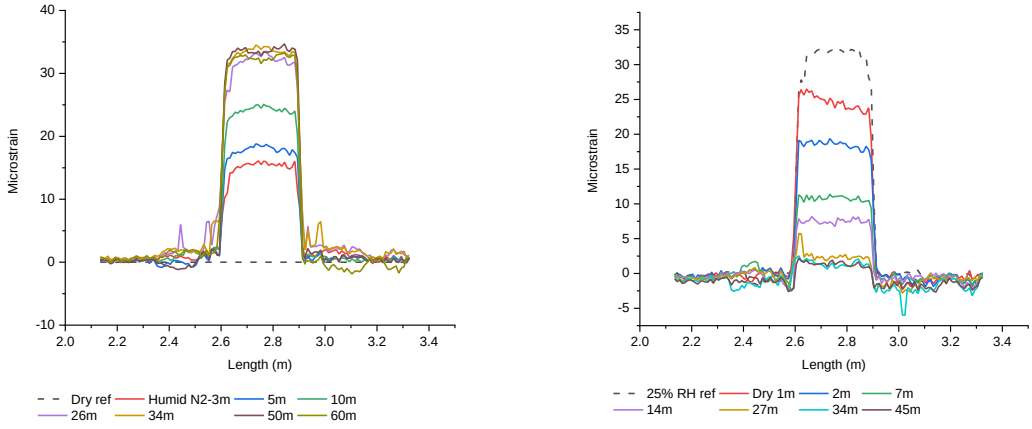

Figure A 7. Reversible at 25% RH

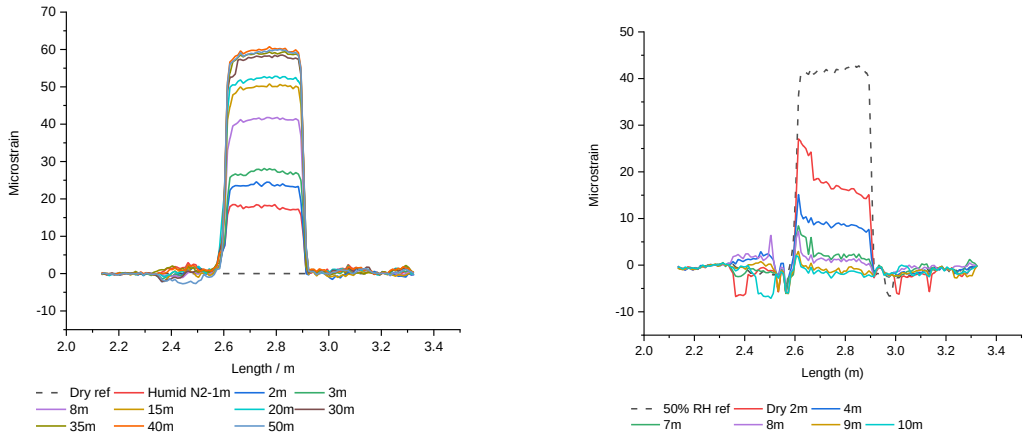

Figure A 8. Reversible at 50% RH

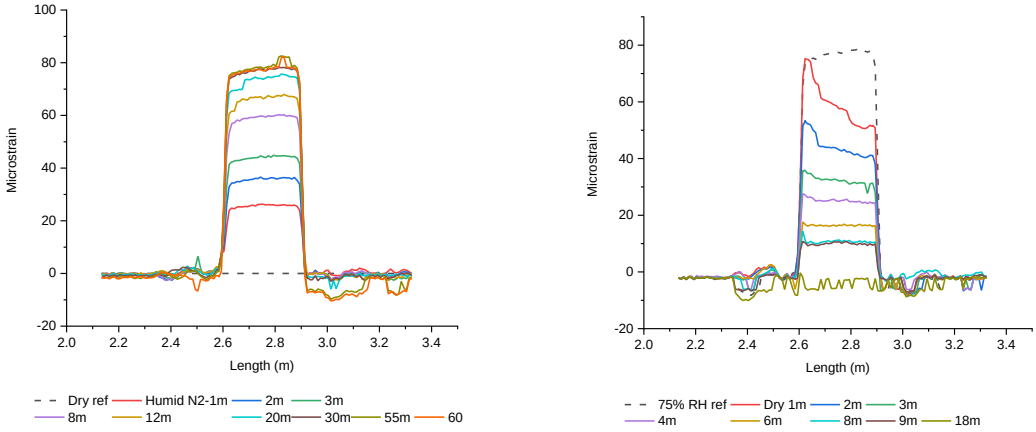

Figure A 9. Reversible at 75% RH

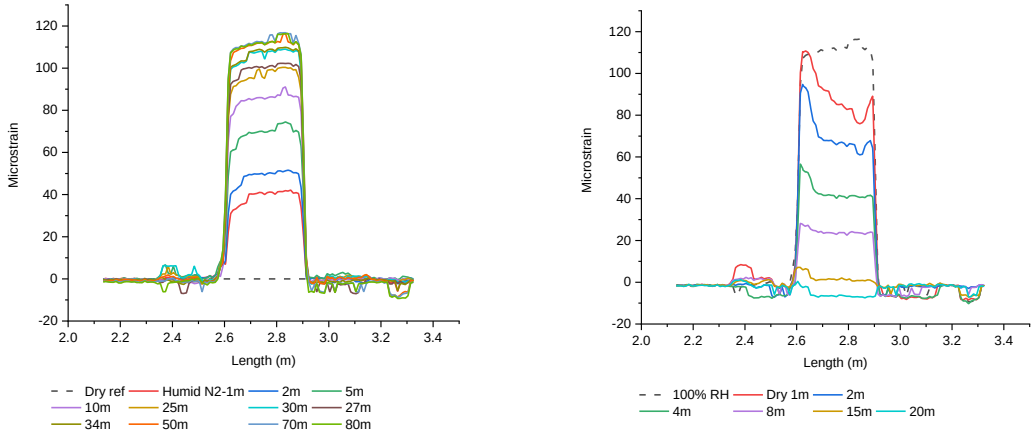

Figure A 10. Reversible at 100% RH

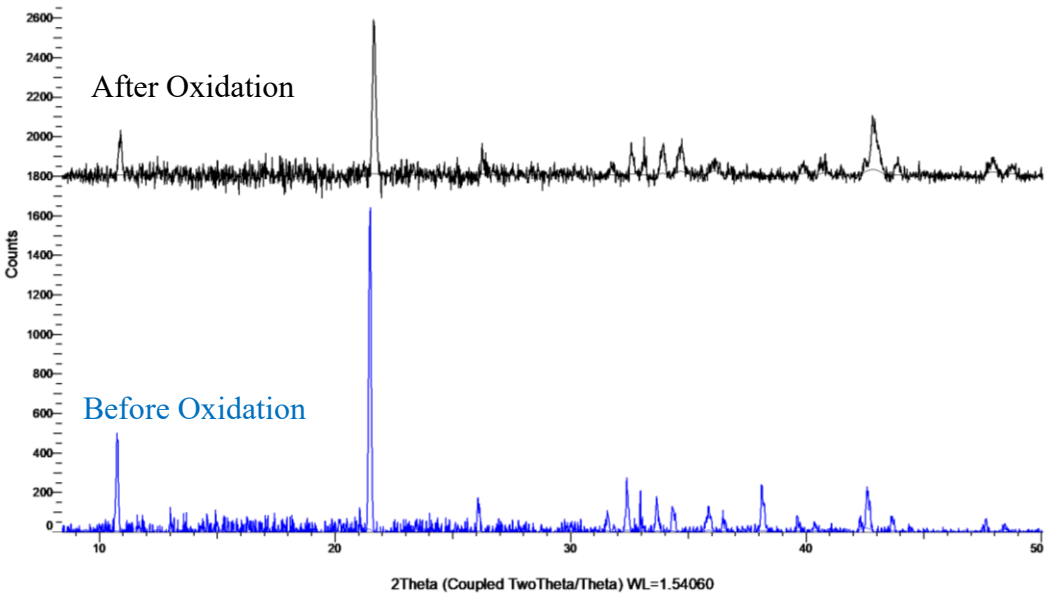

Figure A 11. XRD patterns of oxidation of $Rb_xV_5S_8$ with I_2; before (bottom) and after (top).

LITERATURE CITED

(1) Mallory, G. O.; Hajdu, J. B. *Electroless Plating : Fundamentals and Applications*, Reprint ed.; Mallory, G. O., Hajdu, J. B., Eds.; New York : Noyes Publications/William Andrew Publishing, **1990**.

(2) Wright, R. F.; Lu, P.; Devkota, J.; Fei, L.; Ziomek-Moroz, M.; Ohodnicki, P. R. Review on Corrosion Sensors for Structural Health Monitoring of Oil and Natural Gas Infrastructure; Proc. SPIE 10973, Smart Structures and NDE for Energy Systems and Industry 4.0, 109730N, **2019**. https://doi.org/10.1117/12.2514398.

(3) Ohno, I. Anodic Oxidation of Reductants in Electroless Plating. *J. Electrochem. Soc.* **2006**, *132* (10), 2323. https://doi.org/10.1149/1.2113572.

(4) Georgieva, J.; Armyanov, S. Factors Affecting the Electroless Deposition of Ni-Cu-P Coatings. *J. Electrochem. Soc.* **2003**, *150* (11), C760. https://doi.org/10.1149/1.1612504.

(5) Gan, X.; Zhou, K.; Hu, W.; Zhang, D. Role of Additives in Electroless Copper Plating Using Hypophosphite as Reducing Agent. *Surf. Coatings Technol.* **2012**, *206* (15), 3405–3409. https://doi.org/10.1016/j.surfcoat.2012.02.006.

(6) Li, C. L.; Zhao, H. X.; Tsuru, T.; Zhou, D.; Matsumura, M. Recovery of Spent Electroless Nickel Plating Bath by Electrodialysis. *J. Memb. Sci.* **1999**, *157* (2), 241–249. https://doi.org/10.1016/S0376-7388(98)00381-0.

(7) Malecki, A.; Micek-Ilnicka, A. Electroless Nickel Plating from Acid Bath. *Surf. Coatings Technol.* **2000**, *123* (1), 72–77. https://doi.org/10.1016/S0257-8972(99)00423-5.

(8) Liu, W.; Qiao, X.; Liu, S.; Shi, S.; Liang, K.; Tang, L. A New Process for Pre-Treatment of Electroless Copper Plating on the Surface of Mica Powders with Ultrasonic and Nano-Nickel. **2019**. https://doi.org/10.1016/j.jallcom.2019.03.360.

(9) Wangyu, H.; Bangwei, Z. Electroless Deposition of Iron-Boron Alloys. *Trans. IMF* **1993**, *71* (1), 30–33. https://doi.org/10.1080/00202967.1993.11870979.

(10) Dinderman, M. A.; Dressick, W. J.; Kostelansky, C. N.; Price, R. R.; Qadri, S. B.; Schoen, P. E. Electroless Plating of Iron onto Cellulose Fibers. *Chem. Mater.* **2006**, *18* (18), 4361–4368. https://doi.org/10.1021/cm060649o.

(11) Ohno, I. Electrochemistry of Electroless Plating. *Mater. Sci. Eng. A* **1991**, *146* (1–2), 33–49. https://doi.org/10.1016/0921-5093(91)90266-P.

(12) Fujita, N.; Tanaka, A.; Makino, E.; Squire, P.; Lim, P.; Inoue, M.; Fujii, T. Fabrication of Amorphous Iron-Boron Films by Electroless Plating. *Appl. Surf. Sci.* **1997**, *113–114*, 61–65. https://doi.org/10.1016/S0169-4332(96)00841-0.

(13) Balaraju, J. N.; Rajam, K. S. Electroless Deposition of Ni-Cu-P, Ni-W-P and Ni-W-Cu-P Alloys. **2004**. https://doi.org/10.1016/j.surfcoat.2004.07.068.

(14) Wang, S.-L. Studies of Electroless Plating of Ni-Fe-P Alloys and the Influences of Some Deposition Parameters on the Properties of the Deposits. **2004**. https://doi.org/10.1016/j.surfcoat.2004.01.017.

(15) Cheng, Y. H.; Zou, Y.; Cheng, L.; Liu, W. Effect of Complexing Agents on Properties of Electroless Ni–P Deposits. *Mater. Sci. Technol.* **2008**, *24* (4), 457–460. https://doi.org/10.1179/174328408X281886.

(16) Jin, Y.; Yu, H.; Yang, D.; Sun, D. Effects of Complexing Agents on Acidic Electroless Nickel Deposition. *Rare Met.* **2010**, *29* (4), 401–406. https://doi.org/10.1007/s12598-010-0138-8.

(17) Ahmadi Ashtiani, A.; Faraji, S.; Amjad Iranagh, S.; Faraji, A. H. The Study of Electroless Ni–P Alloys with Different Complexing Agents on Ck45 Steel Substrate. *Arab. J. Chem.* **2017**, *10*, S1541–S1545. https://doi.org/10.1016/j.arabjc.2013.05.015.

(18) Cui, G.; Li, N.; Li, D.; Chi, M. Study of Optimized Complexing Agent for Low-Phosphorus Electroless Nickel Plating Bath. *J. Electrochem. Soc.* **2005**, *152* (10), C669. https://doi.org/10.1149/1.2001487.

(19) Hu, B.; Sun, R.; Yu, G.; Liu, L.; Xie, Z.; He, X.; Zhang, X. Effect of Bath PH and Stabilizer on Electroless Nickel Plating of Magnesium Alloys. **2013**. https://doi.org/10.1016/j.surfcoat.2013.04.011.

(20) Anik, T.; Touhami, M. E.; Himm, K.; Schireen, S.; Belkhmima, R. A.; Abouchane, M.; Cissé, M. *Influence of PH Solution on Electroless Copper Plating Using Sodium Hypophosphite as Reducing Agent*; 2012; Vol. 7.

(21) Sudagar, J.; Lian, J.; Sha, W. Electroless Nickel, Alloy, Composite and Nano Coatings Â€“ A Critical Review. **2013**. https://doi.org/10.1016/j.jallcom.2013.03.107.

(22) Chen, H.; Tai, Y.; Xu, C. Fabrication of Copper-Coated Glass Fabric Composites through Electroless Plating Process. *J. Mater. Sci. Mater. Electron.* **2017**, *28* (1), 798–802. https://doi.org/10.1007/s10854-016-5592-0.

(23) Pang, J. N.; Jiang, S. W.; Lin, H.; Wang, Z. Q. Significance of Sensitization Process in Electroless Deposition of Ni on Nanosized Al 2 O 3 Powders. *Ceram. Int.* **2018**, *42*, 4491–4497. https://doi.org/10.1016/j.ceramint.2015.11.137.

(24) Ohodnicki, P. R.; Natesakhawat, S.; Baltrus, J. P.; Howard, B.; Brown, T. D. Characterization of Optical, Chemical, and Structural Changes upon Reduction of Sol–Gel Deposited SnO2 Thin Films for Optical Gas Sensing at High Temperatures. *Thin Solid Films* **2012**, *520* (19), 6243–6249. https://doi.org/10.1016/J.TSF.2012.05.023.

(25) Wei, X.; Roper, D. K. Tin Sensitization for Electroless Plating Review. *J. Electrochem. Soc.* **2014**, *161* (5), D235–D242. https://doi.org/10.1149/2.047405jes.

(26) Emmanuel Delamarche, *,†; James Vichiconti, ‡; Shawn A. Hall, ‡; Matthias Geissler, †; William Graham, ‡; Bruno Michel, † and; Nunes‡, R. Electroless Deposition of Cu on Glass and Patterning with Microcontact Printing. **2003**. https://doi.org/10.1021/LA034748H.

(27) Nobari, N.; Behboudnia, M.; Maleki, R. Palladium-Free Electroless Deposition of Pure Copper Film on Glass Substrate Using Hydrazine as Reducing Agent. *Appl. Surf. Sci.* **2016**. https://doi.org/10.1016/j.apsusc.2016.05.033.

(28) Krulik, G. A. Electroless Plating of Plastics. *J. Chem. Educ.* **1978**, *55* (6), 361. https://doi.org/10.1021/ed055p361.

(29) Wang, K.; Dong, Y.; Zhang, W.; Zhang, S.; Li, J. Preparation of Stable Superhydrophobic Coatings on Wood Substrate Surfaces via Mussel-Inspired Polydopamine and Electroless Deposition Methods. *Polymers (Basel).* **2017**, *9* (12), 218. https://doi.org/10.3390/polym9060218.

(30) Luiza, B.; Véronique, V.; Fabienne, D. Materials and Manufacturing Processes Influence of the Anionic Part of the Stabilizer on Electroless Nickel-Boron Plating Influence of the Anionic Part of the Stabilizer on Electroless Nickel-Boron Plating. *Mater. Manuf. Process.* **2018**, *33* (2), 227–231. https://doi.org/10.1080/10426914.2017.1291949.

(31) Brenner, A.; Riddell, G. E. Nickel Plating on Steel by Chemical Reduction. *J. Res. Natl. Bur. Stand. (1934).* **2012**, *37* (1), 31. https://doi.org/10.6028/jres.037.019.

(32) Cavallotti, P.; Salvago, G. Studies on Chemical Reduction of Nickel and Cobalt by Hypophosphite. Characteristics of the Process. *Electrochim Met.* **1968**, *3*, 239–266.

(33) Rondin, J.-P.; Hintermann, H. E. A Calorimetric Study of the Electroless Deposition of Nickel. *J. Electrochem. Soc.* **1970**, *117* (2), 160. https://doi.org/10.1149/1.2408405.

(34) Sharma, A.; Cheon, C.-S.; Jung, J. P. Recent Progress in Electroless Plating of Copper. *J. Microelectron. Packag. Soc.* **2017**, *23* (4), 1–6. https://doi.org/10.6117/kmeps.2016.23.4.001.

(35) Hoor, S.; Ahmed, M. F.; Mayana, S. M. *Electroless Deposition of Fe-P, Fe-P-Pt Alloys*; 2000; Vol. 7.

(36) Fessler, R. Pipeline Corrosion, Final Report. *U.S. Dep. Transp. Pipeline Hazard. Mater. Saf. Adminstration Off. Pipeline Saf.* **2008**.

(37) Lu, P.; Wright, R. F.; Ziomek-Moroz, M.; Buric, M. P.; Zandhuis, P.; Ohodnicki, P. R. A Multifunctional Fiber Optic Sensor for Internal Corrosion Monitoring in Natural Gas Transmission Pipelines. **2018**.

(38) Ohodnicki Jr., P. R.; Brown, T. D.; Holcomb, G. R.; Tylczak, J.; Schultz, A. M.; Baltrus, J. P. High Temperature Optical Sensing of Gas and Temperature Using Au-Nanoparticle Incorporated Oxides. *Sensors Actuators B Chem.* **2014**, *202*, 489–499. https://doi.org/10.1016/J.SNB.2014.04.106.

(39) Ohodnicki, P. R.; Wang, C. Optical Waveguide Modeling of Refractive Index Mediated PH Responses in Silica Nanocomposite Thin Film Based Fiber Optic Sensors. *J. Appl. Phys.* **2016**, *119* (6), 064502. https://doi.org/10.1063/1.4941103.

(40) Yan, A.; Poole, Z. L.; Chen, R.; Leu, P. W.; Ohodnicki, P.; Chen, K. P. Scalable Fabrication of Metal Oxide Functional Materials and Their Applications in High-Temperature Optical Sensing. *JOM* **2015**, *67* (1), 53–58. https://doi.org/10.1007/s11837-014-1235-1.

(41) Wang, C.; Ohodnicki, P. R.; Su, X.; Keller, M.; Brown, T. D.; Baltrus, J. P. Novel Silica Surface Charge Density Mediated Control of the Optical Properties of Embedded Optically Active Materials and Its Application for Fiber Optic PH Sensing at Elevated Temperatures. *Nanoscale* **2015**, *7* (6), 2527–2535. https://doi.org/10.1039/c4nr06232a.

(42) OBR 4600 | Luna https://lunainc.com/product/sensing-solutions/obr-4600/ (accessed Jul 9, 2019).

(43) Optical Backscatter Reflectometer 4600 User Guide. 2013.

(44) Wright, R. F.; Egbu, J.; Lu, P.; Buric, M.; Ziomek-Moroz, M.; Ohodnicki, P. R. J. Electrolessly Coated Optical Fibers for Distributed Corrosion Monitoring. In *CORROSION 2019*; NACE International: Nashville, 2019; p No. 13499.

(45) Wright, R.; Badar, M.; Egbu, J. C.; Lu, P.; Buric, M. P.; Ohodnicki, P. R. Fully Distributed Optical Fiber Sensor for Water and Humidity Monitoring. In *Fiber Optic Sensors and Applications XVI*; SPIE, 2019; Vol. 11000, p 6. https://doi.org/10.1117/12.2519239.

(46) Thomas, P. J.; Hellevang, J. O. A Fully Distributed Fibre Optic Sensor for Relative Humidity Measurements. *Sensors Actuators, B Chem.* **2017**. https://doi.org/10.1016/j.snb.2017.02.027.

(47) Hirtenstein, A. How to Mine Cobalt Without going to Congo https://www.bloomberg.com/news/articles/2017-12-01/the-cobalt-crunch-for-electric-cars-could-be-solved-in-suburbia (accessed Jun 18, 2019). https://doi.org/https://www.bloomberg.com/news/articles/2017-12-01/the-cobalt-crunch-for-electric-cars-could-be-solved-in-suburbia.

(48) Goodenough, J. B. Evolution of Strategies for Modern Rechargeable Batteries. *Acc. Chem. Res.* **2013**, *46* (5), 1053–1061. https://doi.org/10.1021/ar2002705.

(49) Kim, H. S.; Arthur, T. S.; Allred, G. D.; Zajicek, J.; Newman, J. G.; Rodnyansky, A. E.; Oliver, A. G.; Boggess, W. C.; Muldoon, J. Structure and Compatibility of a Magnesium Electrolyte with a Sulphur Cathode. *Nat. Commun.* **2011**, *2* (1), 427. https://doi.org/10.1038/ncomms1435.

(50) Aurbach, D.; Lu, Z.; Schechter, A.; Gofer, Y.; Gizbar, H.; Turgeman, R.; Cohen, Y.; Moshkovich, M.; Levi, E. Prototype Systems for Rechargeable Magnesium Batteries. *Nature* **2000**, *407* (6805), 724–727. https://doi.org/10.1038/35037553.

(51) Rong, Z.; Malik, R.; Canepa, P.; Sai Gautam, G.; Liu, M.; Jain, A.; Persson, K.; Ceder, G. Materials Design Rules for Multivalent Ion Mobility in Intercalation Structures. *Chem. Mater.* **2015**, *27* (17), 6016–6021. https://doi.org/10.1021/acs.chemmater.5b02342.

(52) Canepa, P.; Bo, S.-H.; Sai Gautam, G.; Key, B.; Richards, W. D.; Shi, T.; Tian, Y.; Wang, Y.; Li, J.; Ceder, G. High Magnesium Mobility in Ternary Spinel Chalcogenides. *Nat. Commun.* **2017**, *8* (1), 1759. https://doi.org/10.1038/s41467-017-01772-1.

(53) Schramm, W.; Schöllhorn, R.; Eckert, H.; Müller-Warmuth, W. Nonstoichiometric Channel Chalcogenides T1xV5S8: Topotactic Redox Reactions and NMR Studies. *Mater. Res. Bull.* **1983**, *18* (10), 1283–1289. https://doi.org/10.1016/0025-5408(83)90032-6.

(54) Fournès, L.; Vlasse, M.; Saux, M. Preparation, Properties and Crystal Structure of TlV5S8. *Mater. Res. Bull.* **1977**, *12* (1), 1–5. https://doi.org/10.1016/0025-5408(77)90081-2.

(55) Funahashi, S.; Nozaki, H.; Kawada, I. Magnetic Structure of V5S8. *J. Phys. Chem. Solids* **1981**, *42* (11), 1009–1013. https://doi.org/10.1016/0022-3697(81)90064-0.

(56) Egbu, J.; Martin, B. Ion Intercalation into Vanadium Sulfides for Battery Applications. *ECS Meet. Abstr.* **2018**, *MA2018-03* (4), 251–251.

(57) Elgrishi, N. N.; Rountree, K. J.; Mccarthy, B. D.; Rountree, E. S.; Eisenhart, T. T.; Dempsey, J. L. A Practical Beginner's Guide to Cyclic Voltammetry. **2017**. https://doi.org/10.1021/acs.jchemed.7b00361.

(58) Baur, J. E. Diffusion Coefficients. *Handb. Electrochem.* **2007**, 829–848. https://doi.org/10.1016/B978-044451958-0.50036-7.